NASA/TM-20210010977

A Saltation Sensor for the Martian Aqueous Habitat Reconnaissance Suite (MAHRS)

Lawrence Greer and Mike Krasowski
Glenn Research Center, Cleveland, Ohio

August 2021

NASA STI Program . . . in Profile

Since its founding, NASA has been dedicated to the advancement of aeronautics and space science. The NASA Scientific and Technical Information (STI) Program plays a key part in helping NASA maintain this important role.

The NASA STI Program operates under the auspices of the Agency Chief Information Officer. It collects, organizes, provides for archiving, and disseminates NASA's STI. The NASA STI Program provides access to the NASA Technical Report Server—Registered (NTRS Reg) and NASA Technical Report Server—Public (NTRS) thus providing one of the largest collections of aeronautical and space science STI in the world. Results are published in both non-NASA channels and by NASA in the NASA STI Report Series, which includes the following report types:

- TECHNICAL PUBLICATION. Reports of completed research or a major significant phase of research that present the results of NASA programs and include extensive data or theoretical analysis. Includes compilations of significant scientific and technical data and information deemed to be of continuing reference value. NASA counter-part of peer-reviewed formal professional papers, but has less stringent limitations on manuscript length and extent of graphic presentations.

- TECHNICAL MEMORANDUM. Scientific and technical findings that are preliminary or of specialized interest, e.g., "quick-release" reports, working papers, and bibliographies that contain minimal annotation. Does not contain extensive analysis.

- CONTRACTOR REPORT. Scientific and technical findings by NASA-sponsored contractors and grantees.

- CONFERENCE PUBLICATION. Collected papers from scientific and technical conferences, symposia, seminars, or other meetings sponsored or co-sponsored by NASA.

- SPECIAL PUBLICATION. Scientific, technical, or historical information from NASA programs, projects, and missions, often concerned with subjects having substantial public interest.

- TECHNICAL TRANSLATION. English-language translations of foreign scientific and technical material pertinent to NASA's mission.

For more information about the NASA STI program, see the following:

- Access the NASA STI program home page at http://www.sti.nasa.gov

- E-mail your question to help@sti.nasa.gov

- Fax your question to the NASA STI Information Desk at 757-864-6500

- Telephone the NASA STI Information Desk at 757-864-9658

- Write to:
  NASA STI Program
  Mail Stop 148
  NASA Langley Research Center
  Hampton, VA 23681-2199

NASA/TM-20210010977

A Saltation Sensor for the Martian Aqueous Habitat Reconnaissance Suite (MAHRS)

Lawrence Greer and Mike Krasowski
Glenn Research Center, Cleveland, Ohio

National Aeronautics and
Space Administration

Glenn Research Center
Cleveland, Ohio 44135

August 2021

Acknowledgments

We would like to extend a special thanks to Gustave C. Fralick for providing the computations for the particle velocity with air resistance. We would also like to thank Adam C. Wroblewski for providing the computational flow dynamic simulations for the wind tunnel. Lastly, we would like to acknowledge the contributions of Norman F. Prokop and the SMiRF facility personnel toward the successful completion of the environmental testing of the saltation sensor.

Level of Review: This material has been technically reviewed by technical management.

Available from

NASA STI Program
Mail Stop 148
NASA Langley Research Center
Hampton, VA 23681-2199

National Technical Information Service
5285 Port Royal Road
Springfield, VA 22161
703-605-6000

This report is available in electronic form at http://www.sti.nasa.gov/ and http://ntrs.nasa.gov/

A Saltation Sensor for the Martian Aqueous Habitat Reconnaissance Suite (MAHRS)

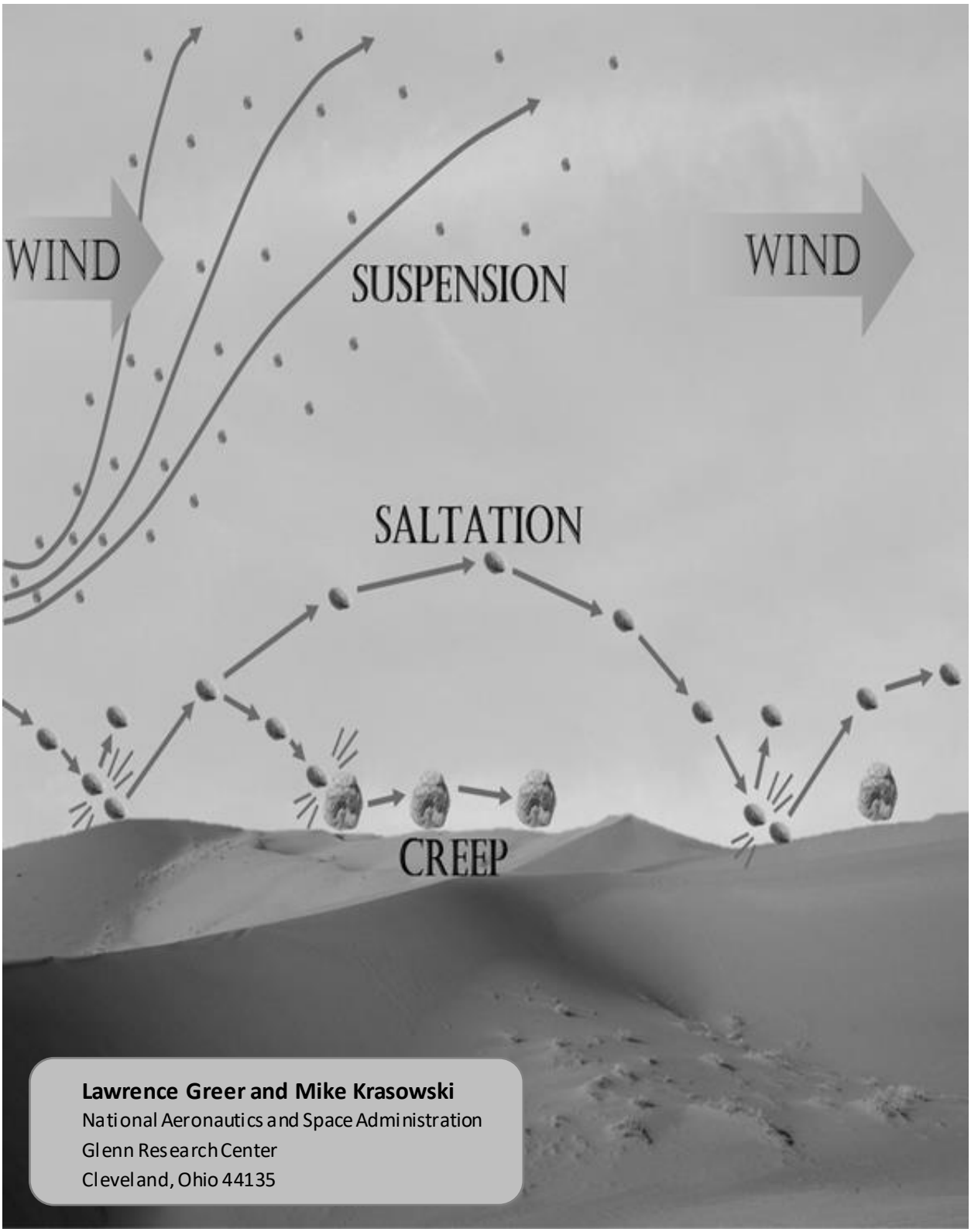

Lawrence Greer and Mike Krasowski
National Aeronautics and Space Administration
Glenn Research Center
Cleveland, Ohio 44135

Saltation Sensor Overview

Wind-blown sand, otherwise known as saltation, occurs on the surface of Mars, but its characteristics are poorly understood due to insufficient data *(Kok, 2010)*. Space-qualified instrumentation for acquiring saltation data is unavailable, making it difficult to advance our knowledge in this area. Consequently, a saltation sensor probe with supporting electronics was designed and constructed with a clear path to space readiness in order to support future science missions to the Martian surface for advancing the understanding of Martian saltation *(figure 1a)*.

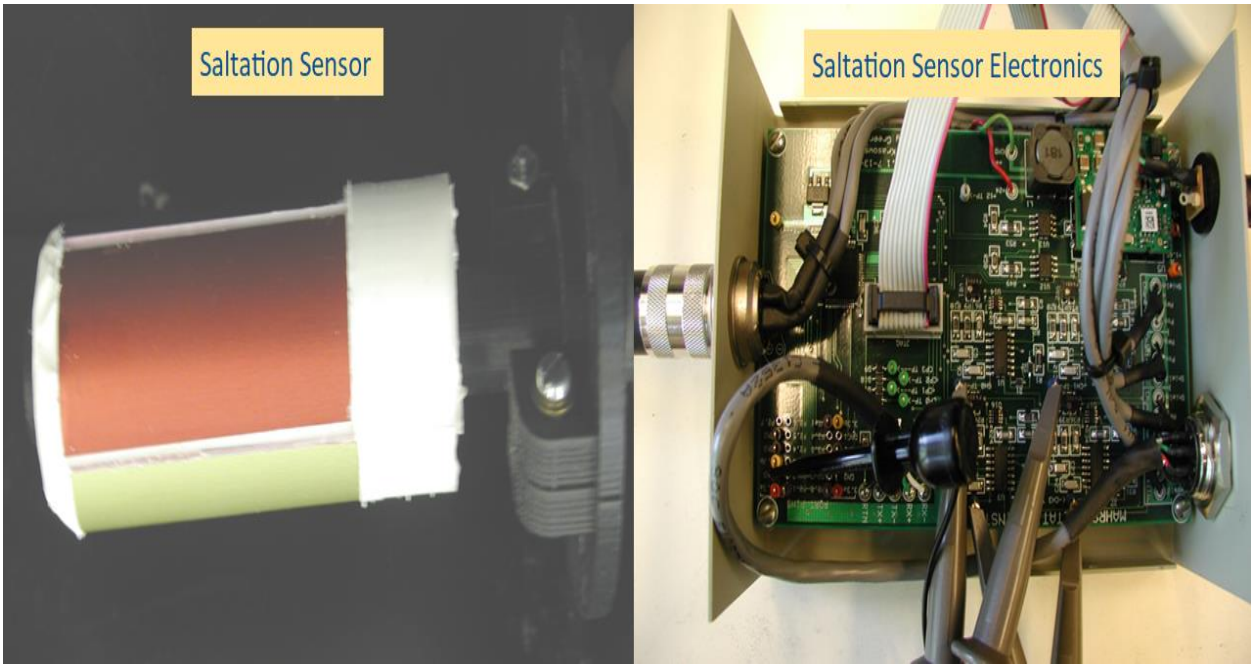

Figure 1a *– Saltation Sensor and Electronics Box.*

Saltation Sensor Probe Design

The saltation sensor is designed around a thin-film piezoelectric appliance in order to take advantage of the excellent sensitivity to low energy impacts demonstrated by this family of devices *(Pelt, et al., 2009; Barchyn, et al. 2010)*. It was discovered through experimentation that pre-stressing the piezoelectric thin-film by curving it around a form further heightened its sensitivity. This discovery spawned the design that affixes the piezo-film sensors to the interior of thin-walled aluminum tubing; providing protection from the elements without compromising signal output during low energy particle impacts. An innovative four quadrant design enables coarse measurements on particle flow direction *(figure 1b)*. With this in mind, color-anodized tubing was used to simplify flow direction verification during testing. The four quadrants of the saltation sensor are held together and vibrationally isolated using RTV511 which has an extended temperature range from -115°C to 204°C and is well suited to handle the low Martian temperature extremes. The sensor also incorporates a grounding scheme that makes use of conductive epoxy and copper braid applied to each tube quadrant. This produces a Faraday shield around the piezo elements which greatly improves the EMI performance of the sensor. Electric fields and charged particles might play a significant role in Martian saltation *(Kok, Renno, 2006)* which makes this shielding essential to the prevention of erroneous impact readings. Shock absorbing mounts were also added to provide additional vibration isolation between spacecraft and sensor.

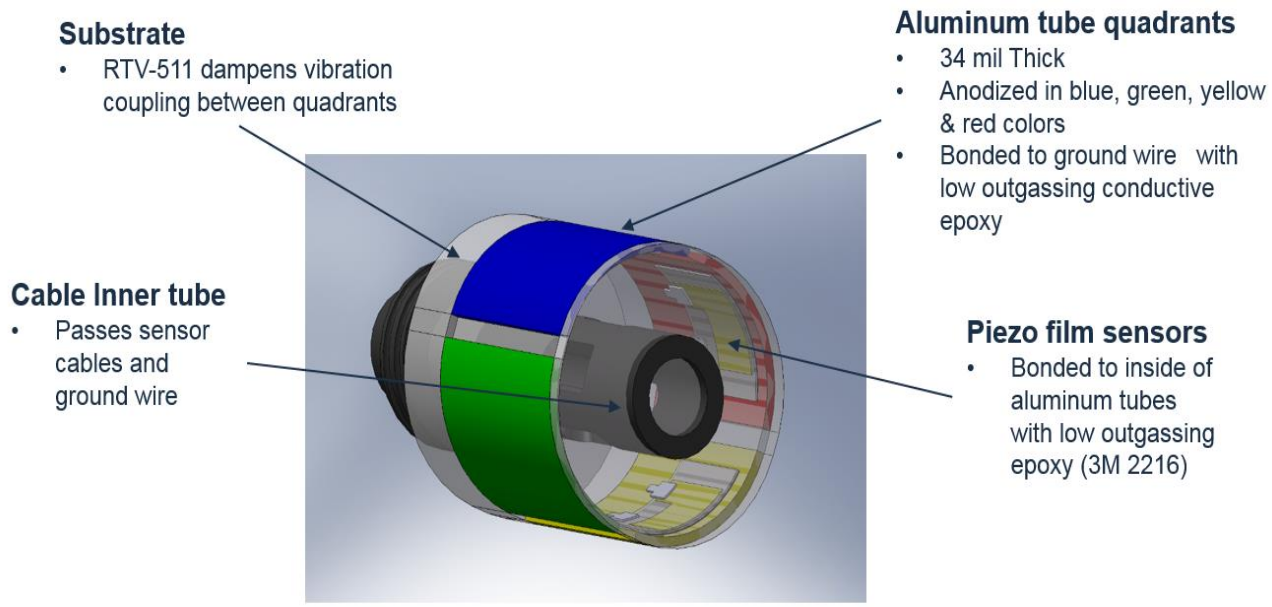

Figure 1b *– CAD drawing of interior of saltation sensor.*

Saltation Sensor Signal Processing

The raw signal from the piezo-electric sensor is comprised of several charge transfers generated from individual impacts. These charges 'pile-up' together forming a waveform that is not conducive to utilizing a simple threshold technique for distinguishing one impact event from another. The pulse reshaping circuitry separates the particle impact signals into Gaussian shaped pulses *(figure 2)* which are easily applied against a threshold to perform impact counting. Furthermore, the pulse peak and the area under each individual reshaped pulse is proportional to the energy level of the impact event.

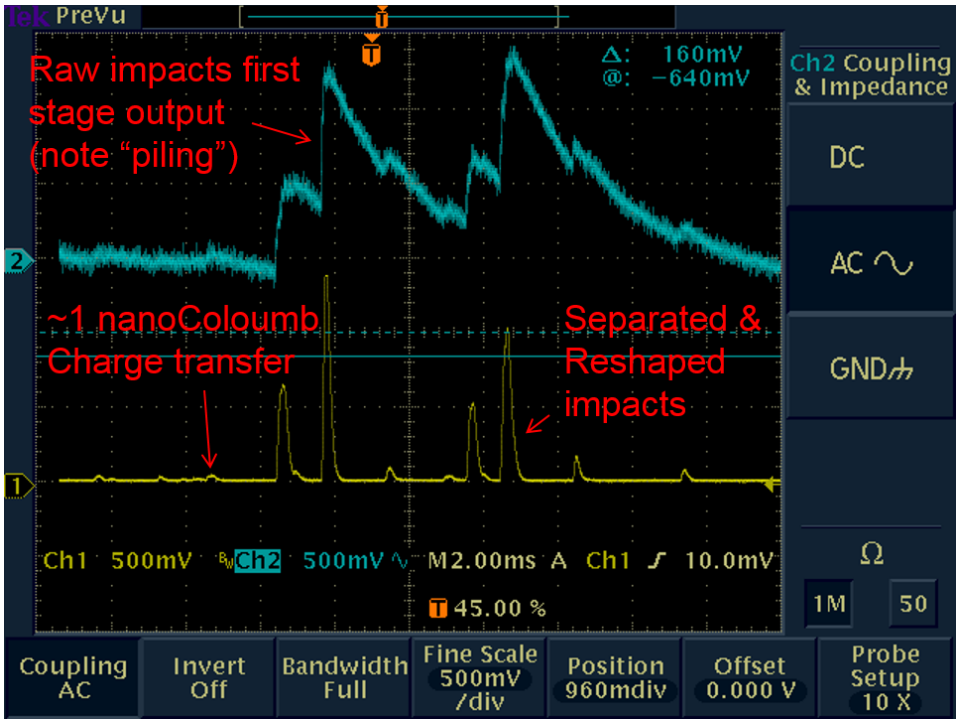

Figure 2 *- Saltation sensor scope trace of sand impacts from 1 cm height.*

The electronics responsible for reshaping the piezoelectric signal *(figure 3)* consists of a charge sensitive, rectifying amplifier stage followed by generic voltage gain stage. Subsequent signal shaping stages follow to reshape the initial charge transfer from an impact on the piezoelectric film to a Gaussian shaped waveform.

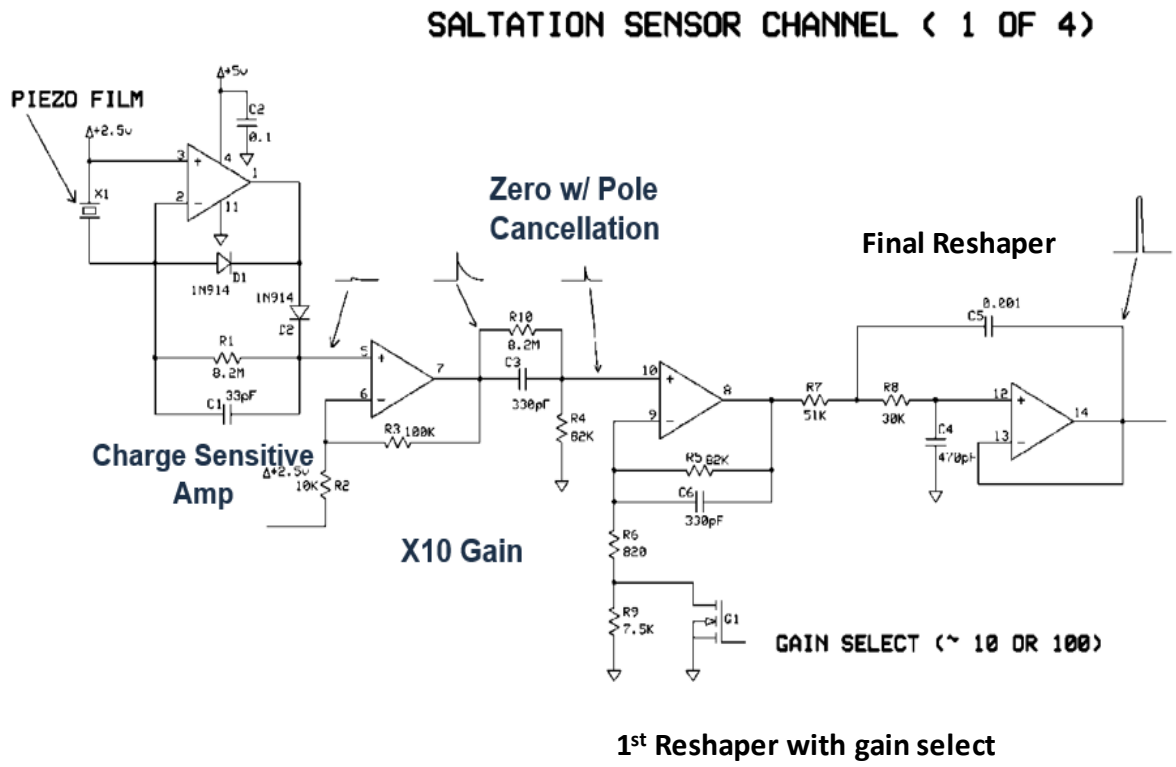

***Figure 3**- Saltation sensor signal conditioning circuit.*

Saltation Sensor Processing Overview

The signal processing electronics designed for the saltation sensor receives the amplified outputs of the pulse-shaping stages of each of the four saltation sensor quadrants. These outputs drive four comparators with user selectable thresholds as well as four channels of a multiplexed 8-bit analog-to-digital converter onboard a Silicon Laboratories 8051 core microcontroller *(figure 4)*. The microcontroller's onboard digital-to-analog converter is used to set the threshold for all four comparators, allowing for a user selectable energy trip point level for the particle impacts. The rising edges from each of the four comparator outputs directly increment four hybrid 32-bit counters onboard the microcontroller at the hardware level in order to record the total number of particle impacts. The lower 16 bits of the hybrid counter are directly clocked in hardware, whereas the upper 16 bits are incremented in an interrupt service routine upon the occurrence of a counter overflow in the corresponding lower word. The outputs of the comparators are also polled by the microcontroller to determine when to capture the constant stream of analog-to-digital conversions performed on each of the four saltation sensor channels which are then used to update the sensor impact statistics. These statistics include the pulse peaks, pulse widths, pulse areas and pulse counts resulting from the particle impacts. In addition to the aforementioned statistics, the microcontroller maintains an energy

spectrum within 256 individual bins: each of which is comprised of a 16-bit wide counter. This feature is known as a pulse-height analyzer in other commercial units *(Sensit, 2013)*. An on-board clock within the microcontroller sets the acquisition timing interval as well as the serial transmission timing interval. In addition to transmitting saltation data to the host through a RS422 communication bus, the serial hardware within the microcontroller also receives commands from the host. These host commands allow alterations of various acquisition testing parameters within the sensor hardware.

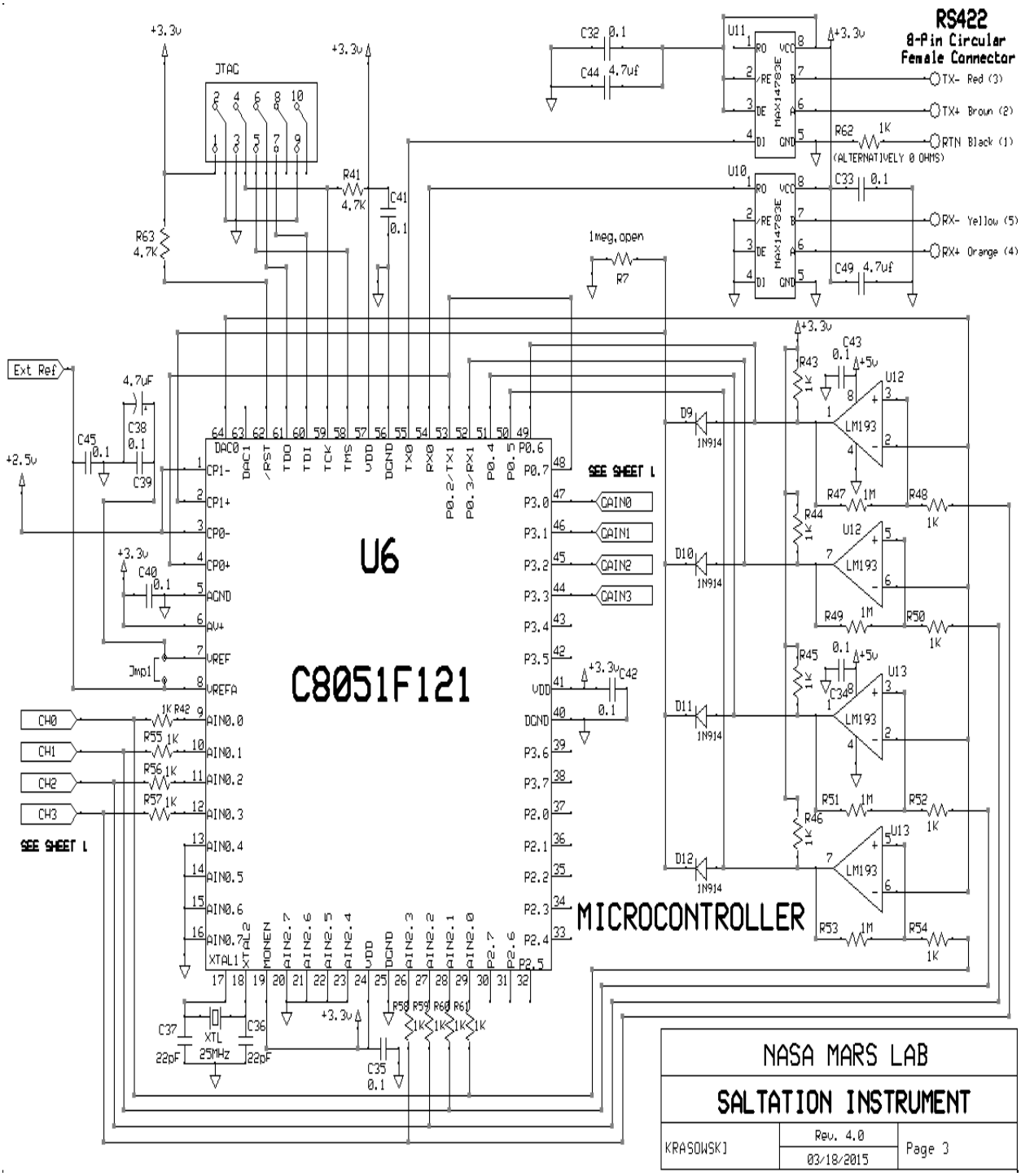

Figure 4 *– Saltation microcontroller core and associated electronics.*

Analog-to-digital conversions performed on the sensor quadrant outputs occur every 16 *µsec* when the sensor signal is above the designated threshold *(figure 5)* or when an 8 *msec* wide waveform capture of the four sensor quadrants is requested. During the former case, once the microcontroller detects that the sensor output is above the designated threshold, it captures the signal every 16 *µsec* until the signal drops below the threshold. At that time, the impact statistics are logged and averaged over a 40 msec window. A serial transmission of the averaged data also occurs on this 40 *msec* interval period.

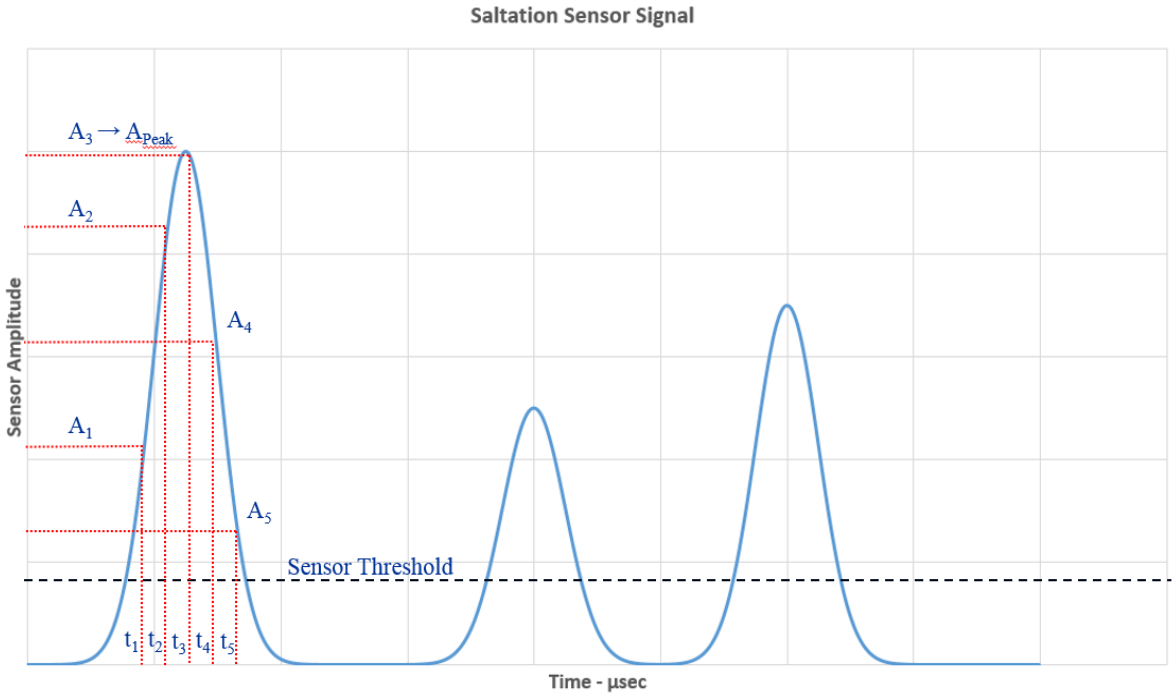

Figure 5 *– Sensor amplitudes $A_1 – A_n$ are captured by the A/D converter while the signal is above the threshold. The time intervals $\Delta t = t_n – t_{n+1}$ are fixed at 16µsec.*

The area under the peaks of the reshaped saltation sensor signal are approximated by the Riemann sum $\sum_{n=0}^{K} A_n \Delta t$ where A_n is the captured signal amplitude level and Δt is the constant time interval between acquisitions. Because an experimentally derived constant will be used to correlate the pulse area or pulse peak with the energy of the sensor impacts, Δt can absorbed within this constant and ultimately discarded during the acquisition. This yields a simple summation $\sum_{n=0}^{K} A_n$ without the added complexity of a multiplication operation. Consequently, only simple math operations are performed such as counting the number (k) of readings that occur while above the threshold, recording the pulse peaks (A_{Peak}) and summing the pulse amplitudes (A_n) while above the threshold. Most of the processing time of the microcontroller is used to acquire and record the sensor information, and these simple math operations (increment, check-if-greater-than and summation) facilitate maximum data throughput whilst handling other required interrupt service routines responsible for channel sequencing, counter overflows, transmitting data and receiving control commands.

Saltation Graphical-User-Interface Overview

The user interface controlling the saltation test apparatus (Saltation Recorder) is a Labview® program consisting of four window panes for manipulating or monitoring various aspects of the saltation sensor, wind tunnel and electronic-scale hardware. The impact capture window pane *(figure 6)* possesses the control interface for selecting the serial communication ports for both the saltation and wind tunnel hardware. It also facilitates selecting the particle energy detection gain and threshold settings, selecting window-averaging or window-maximum acquisition modes, selecting single or continuous waveform capture, resetting the particle counts and requesting an energy spectrum dump to a file. Furthermore, the current state of the saltation sensor hardware is displayed in a status monitoring block adjacent to the control interface. The most recent waveform captures for each of the four saltation sensor quadrants along with the total number of impact counts per quadrant are also displayed in this window pane. Lastly, the averaged particle flow direction is displayed on a polar plot which in conjunction with a color coded key, indicates the particle flow vector relative to the four quadrants of the saltation sensor. The method used to calculate the averaged particle flow direction is shown in *equation 1*.

$$\Theta = \text{Direction of particle flow} = (180/\pi)\, f(y/x) \; ; \quad \begin{aligned} f(y/x) &= \tan^{-1}(y/x), \text{ if } x>0 \\ f(y/x) &= \pi/2, \text{ if } x=0 \text{ and } y>0 \\ f(y/x) &= -\pi/2, \text{ if } x=0 \text{ and } y<0 \\ f(y/x) &= \pi/2 - \tan^{-1}(y/x), \text{ if } x<0 \text{ and } y>0 \\ f(y/x) &= -\pi/2 - \tan^{-1}(y/x), \text{ if } x<0 \text{ and } y<0 \\ \Theta &= \Theta + 360, \text{ if } \Theta < 0 \end{aligned}$$

$$x = (AIE_{Red} - AIE_{Green})/(AIE_{Red} + AIE_{Green} + AIE_{Blue} + AIE_{Yellow});$$
$$y = (AIE_{Blue} - AIE_{Yellow})/(AIE_{Red} + AIE_{Green} + AIE_{Blue} + AIE_{Yellow});$$

AIE_{Blue} = Average Impact Energy on blue sensor face
AIE_{Yellow} = Average Impact Energy on yellow sensor face
AIE_{Red} = Average Impact Energy on red sensor face
AIE_{Green} = Average Impact Energy on green sensor face

Equation 1 *– Calculation of particle flow direction.*

The direction of particle flow "Θ", is derived from the averaged particle impact energies (pulse areas) measured on each of the saltation sensor quadrants. The x-axis is defined as the center-line of the sensor that spans the midpoints between the red and green quadrants; whereas the y-axis is defined by the center-line that spans the midpoints between the blue and yellow quadrants. The width of the time-window used to average the particle impact energies on the quadrants is selectable from 1 to 5 seconds. The longer averaging times yield a more stable albeit less responsive particle flow reading. After the x and y components of the direction vector are calculated from the averaged particle impact energies, a polar plot with a fixed magnitude is generated. The result is a "compass-like" indicator showing the direction of the particle flow impinging on the saltation sensor. This tool proved quite useful during testing because it provided a means to align the sensor in the particle flow, thus maintaining uniform test conditions for each of the sensor quadrants.

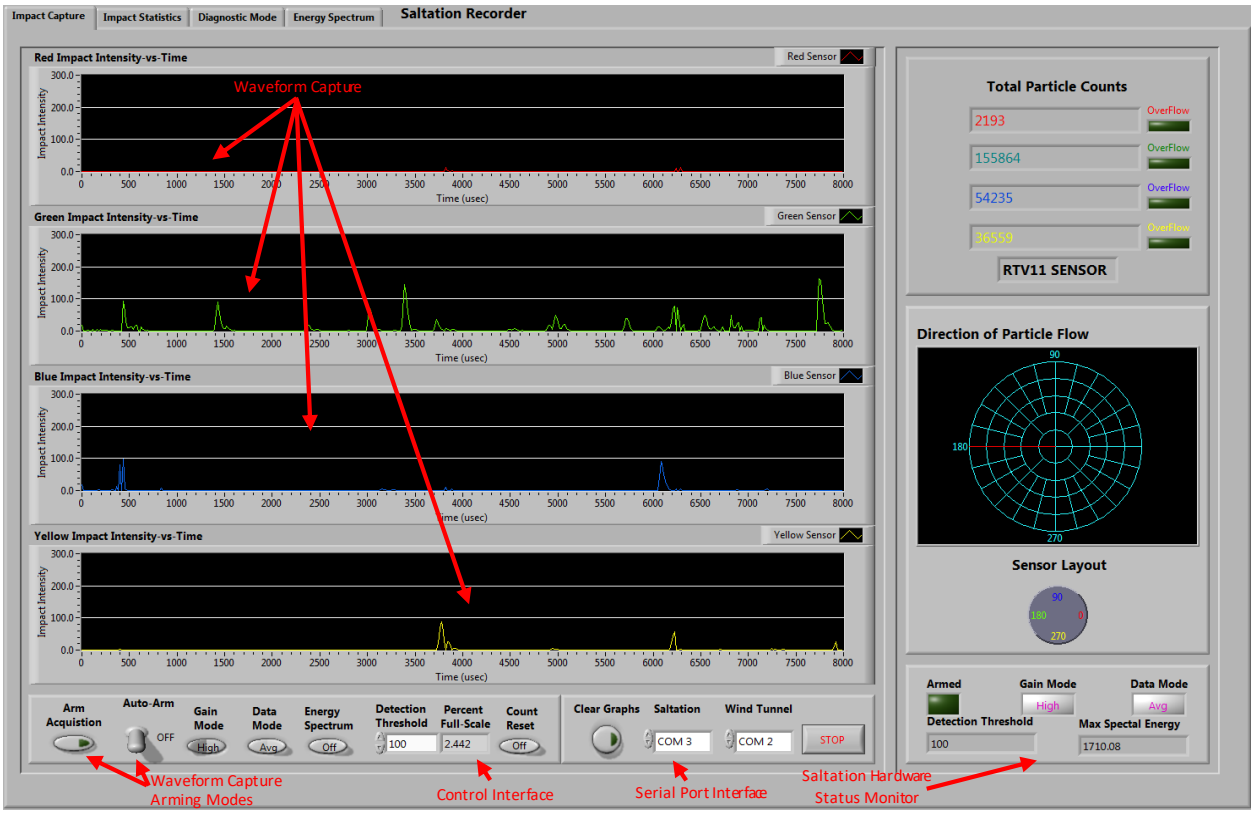

Figure 6 *– Impact capture window pane of LabView® Interface program for Saltation test apparatus.*

The impact statistics window pane *(figure 7)* contains three graphs that display real-time features of the particle impacts averaged within a rolling 40 µsec time window. About every 1.5 seconds, the top graph displays the energy spectrum of the impacts across all four quadrants of the saltation sensor.

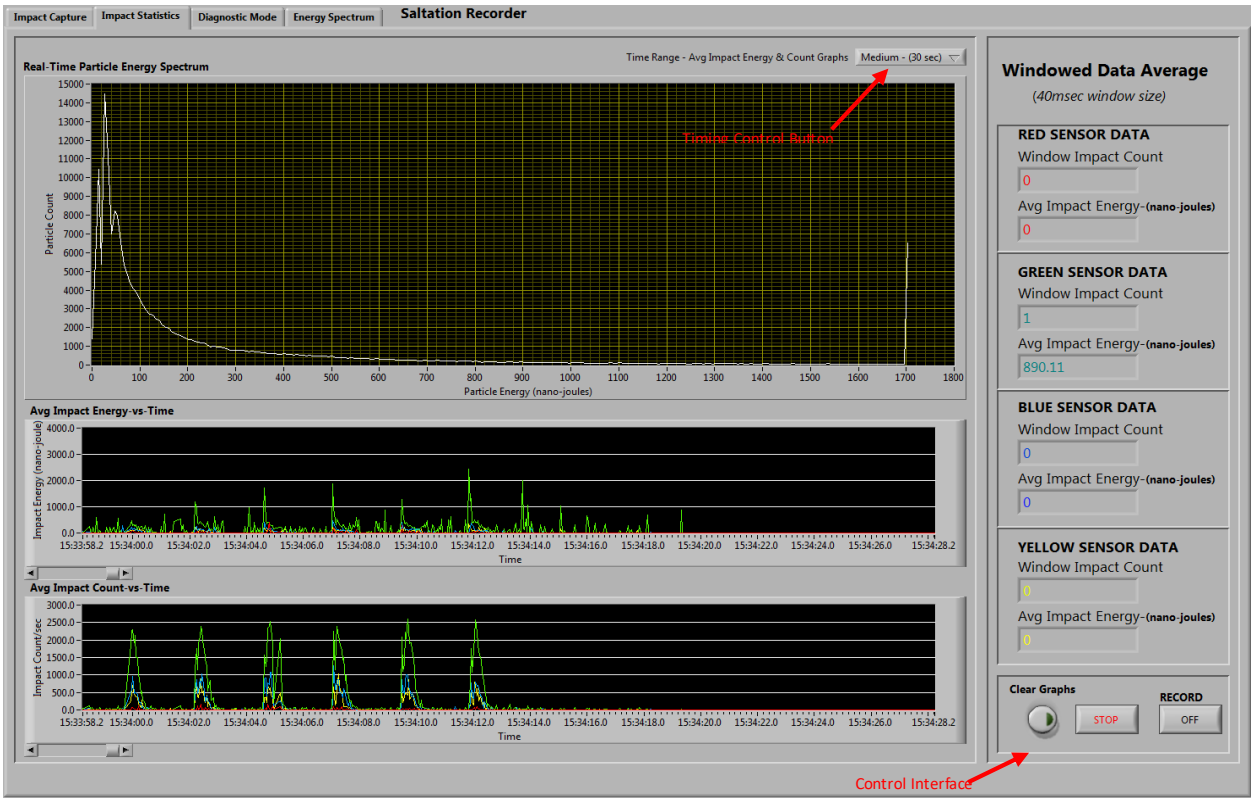

Figure 7 *– Impact statistics window pane of LabView® Interface program for Saltation test apparatus.*

The middle graph shows the average energy of the impacts versus time for each of the four quadrants of the saltation sensor. Lastly, the bottom graph displays the average impact count versus time for each of the four quadrants of the saltation sensor. The time-scale for the middle and bottom graphs can be adjusted to display finer or coarse detail using the time control button near the top of the window pane. The averaged quantities are also displayed numerically for both the particle energy and particle count in the column adjacent to the graphs. Lastly, provision is made to clear the graphs and start or stop recording data to a file through a control interface on the bottom right-hand side of the window pane.

The diagnostic window pane *(figure 8)* allows monitoring and control of each of the three subsystems that comprise the saltation test apparatus: the saltation sensor control hardware, the wind tunnel control hardware and the electronic scale. Due to wiring variations between sensor versions, an allowance was made in the program to select the type of sensor according to its substrate: urethane or RTV11. Also, variations between the versions of the saltation control electronics required a selector for the gain polarity. Other user selectable parameters for the saltation sensor electronics are the time window size used to average the data for the particle flow direction indicator and the spectral energy divisor which determines the bin widths for the spectral energy graph. The serial data streams for the general impact data, impact waveform, energy spectrum and command data output are monitored. Lastly, the particle flow direction parameters are monitored in real-time.

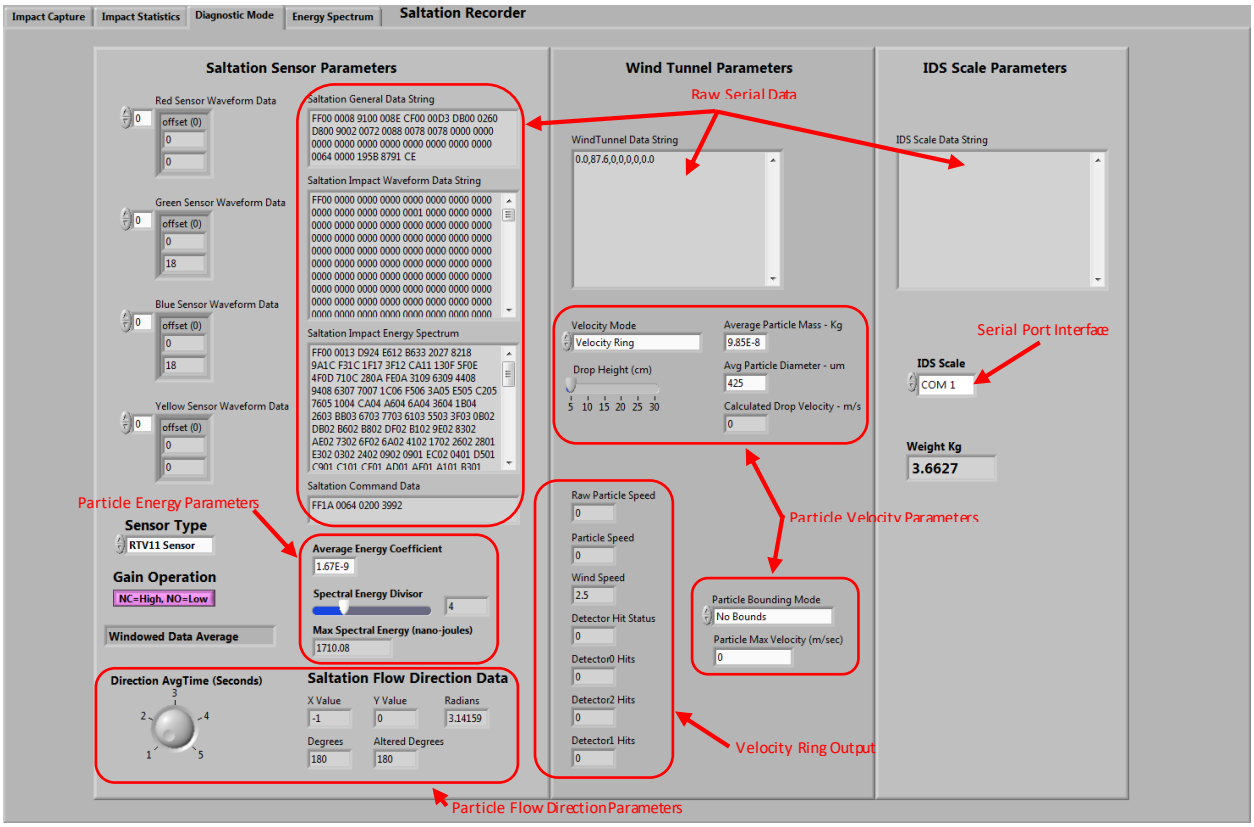

Figure 8 *– Diagnostic mode window pane of LabView® Interface program for Saltation test apparatus.*

The monitor and control operations for the wind tunnel hardware reside in the middle column where either a wind tunnel or flume arrangement can be accommodated. Particle velocity measurements are calculated based on drop heights (used in conjunction with particle volume and mass) or the measured transit-time of particles over a prescribed distance. The wind tunnel arrangement is restricted to using

the velocity ring which uses three sets of dual light-sheet and detector pairs spaced at 120° intervals to determine the transit-time required for a particle to traverse the distance between the detector pairs.

The flume arrangement can use either the velocity ring measurement or the calculated velocity based on drop height. The parameters used for both types of velocity measurements reside this column: velocity mode (choice of the velocity ring or drop parameters), velocity drop parameters (height, mass, diameter) and velocity bounding options (wind speed upper bound, user selected upper bound or unbounded). As with the saltation sensor hardware, the wind tunnel raw serial data stream is monitored and the associated measured outputs are displayed. The electronic scale output is monitored in the last of the columns within the diagnostic mode window pane. The serial port connecting the scale to the computer is also selected within this column. As with the previous hardware specific columns, the electronic scale raw serial data stream is monitored and the real-time mass quantity displayed.

The energy spectrum window pane *(figure 9)* displays an enlarged version of the real-time energy spectrum as shown in the impact statistics window pane. However, the spectrum displayed in this pane is the result of the capture initiated at the time the energy spectrum capture-to-file mode is selected from within the impact capture window pane.

After starting the Saltation Recorder program, the user is prompted to select either the waveform capture or saltation statistics mode and a corresponding file name to store the associated data. A recording of the selected data to the requested file begins once the record button within the impact statistics window pane is activated. Each time an energy spectrum is requested, the user is prompted for a separate file name to store the spectral data, allowing for many captures of the energy spectrum at various points in time.

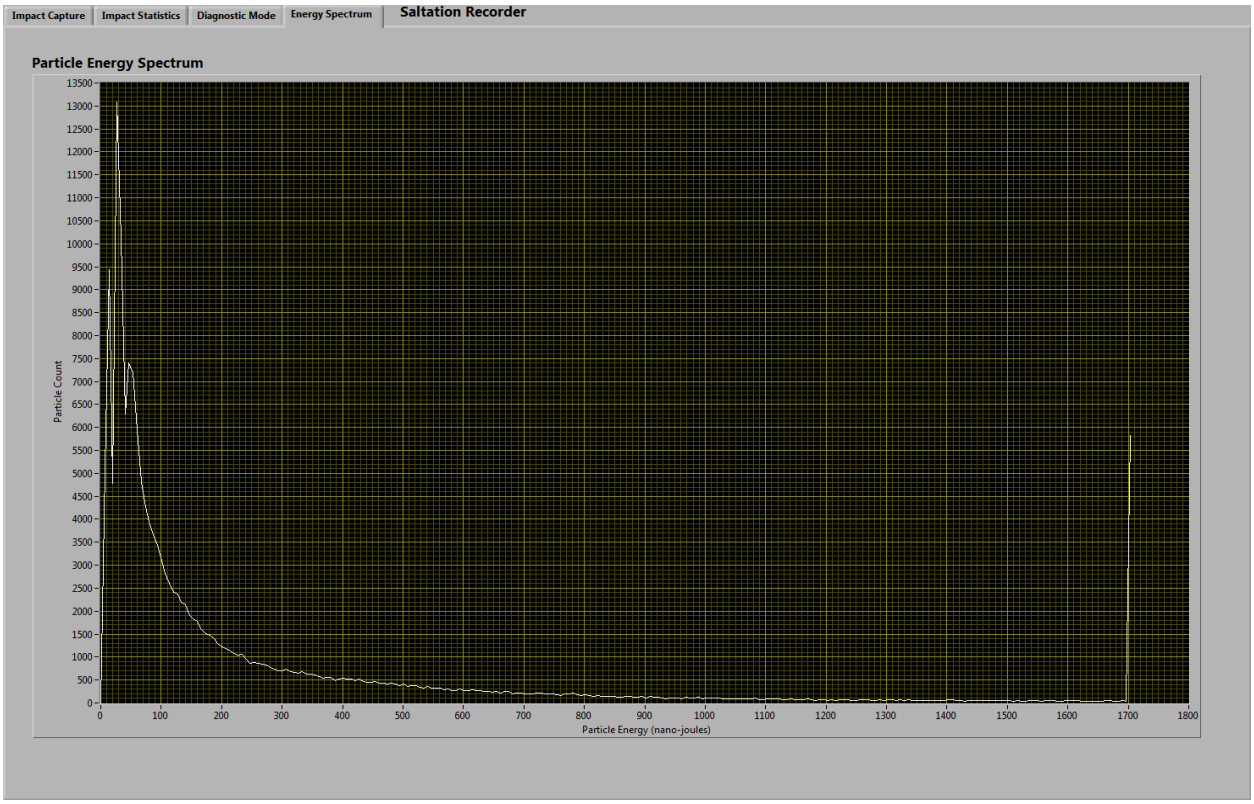

Figure 9 *– Energy spectrum window pane of LabView® Interface program for Saltation test apparatus.*

The collected data from the Saltation Recorder is compatible with the Microsoft Excel® spreadsheet format. Consequently, all data is imported into Excel® where sensor and scale flux rates are calculated and compared *(figure 10)*. Also within Excel® the averaged particle velocities are used to calculate particle energy levels which are correlated to the averaged sensor peak and energy readings in order to determine if a repeatable correlation coefficient is feasible *(figure 11)*.

	A	B	C	D	E	F	G	H
1	Time (s)	Air Velocity (m/s)	Particle Velocity (m/s)	Particle Energy (joules)	Red Impact Energy	Green Impact Energy	Blue Impact Energy	Yellow Impact Energy
2	4.90E+04	-6.00E-01	0.00E+00	0.00E+00	0.00E+00	4.60E+01	0.00E+00	0.00E+00
3	4.90E+04	-6.00E-01	0.00E+00	0.00E+00	0.00E+00	6.80E+01	0.00E+00	0.00E+00
4	4.90E+04	-6.00E-01	0.00E+00	0.00E+00	0.00E+00	8.60E+01	0.00E+00	0.00E+00
5	4.90E+04	-6.00E-01	6.10E+00	1.83E-06	0.00E+00	0.00E+00	0.00E+00	0.00E+00
6	4.90E+04	-6.00E-01	0.00E+00	0.00E+00	0.00E+00	0.00E+00	0.00E+00	0.00E+00
7	4.90E+04	-6.00E-01	0.00E+00	0.00E+00	0.00E+00	1.90E+01	0.00E+00	0.00E+00
8	4.90E+04	-6.00E-01	0.00E+00	0.00E+00	0.00E+00	7.60E+01	6.90E+01	6.60E+01
9	4.90E+04	-6.00E-01	0.00E+00	0.00E+00	0.00E+00	4.40E+01	2.25E+02	6.50E+01
10	4.90E+04	-6.00E-01	0.00E+00	0.00E+00	0.00E+00	9.10E+01	0.00E+00	0.00E+00
11	4.90E+04	-6.00E-01	0.00E+00	0.00E+00	0.00E+00	1.48E+02	0.00E+00	0.00E+00
12	4.90E+04	-6.00E-01	0.00E+00	0.00E+00	0.00E+00	1.49E+02	0.00E+00	0.00E+00

	I	J	K	L	M	N	O	P	Q	R
1	Red Impact Peak	Green Impact Peak	Blue Impact Peak	Yellow Impact Peak	Red Total Count	Green Total Count	Blue Total Count	Yellow Total Count	Velocity Unit Status	IDS Scale Reading (Kg)
2	0.00E+00	1.50E+01	0.00E+00	0.00E+00	3.00E+00	5.11E+03	1.14E+03	5.66E+02	0.00E+00	1.80E-03
3	0.00E+00	2.20E+01	0.00E+00	0.00E+00	3.00E+00	5.11E+03	1.14E+03	5.66E+02	0.00E+00	1.80E-03
4	0.00E+00	2.90E+01	0.00E+00	0.00E+00	3.00E+00	5.12E+03	1.14E+03	5.66E+02	0.00E+00	1.80E-03
5	0.00E+00	2.90E+01	0.00E+00	0.00E+00	3.00E+00	5.12E+03	1.14E+03	5.66E+02	2.00E+00	1.80E-03
6	0.00E+00	2.90E+01	0.00E+00	0.00E+00	3.00E+00	5.12E+03	1.14E+03	5.66E+02	0.00E+00	1.80E-03
7	0.00E+00	9.00E+00	0.00E+00	0.00E+00	3.00E+00	5.13E+03	1.14E+03	5.66E+02	0.00E+00	1.80E-03
8	0.00E+00	9.00E+00	0.00E+00	0.00E+00	3.00E+00	5.14E+03	1.14E+03	5.68E+02	0.00E+00	1.80E-03
9	0.00E+00	1.70E+01	5.20E+01	2.30E+01	3.00E+00	5.14E+03	1.15E+03	5.70E+02	0.00E+00	1.80E-03
10	0.00E+00	2.90E+01	0.00E+00	0.00E+00	3.00E+00	5.15E+03	1.15E+03	5.70E+02	0.00E+00	1.80E-03
11	0.00E+00	2.90E+01	0.00E+00	0.00E+00	3.00E+00	5.16E+03	1.15E+03	5.70E+02	0.00E+00	1.80E-03
12	0.00E+00	4.40E+01	0.00E+00	0.00E+00	3.00E+00	5.16E+03	1.15E+03	5.70E+02	0.00E+00	1.80E-03

Figure 10 *– Saltation data that has been recorded and imported into Excel®.*

	V	W	X	Y	Z	AA
1	Flume Cross-Sectional Area (mm-2)	Sensor Quadrant Cross-Sectional Area (mm-2)	Avg Particle Velociy (m/s)	Avg Particle Energy (Kgm2s-2)	Avg Sensor Pulse Energy	Avg Sensor Pulse Peak
2	4933.86	835	1.604054054	1.2672E-07	95.05190361	30.24784037
3						
4		Full Sensor Quadrant Cross-Sectional Area (mm-2)			Pulse Energy Coefficient	Pulse Peak Coefficient
5		1164			1.33316E-09	4.18938E-09
6						

Figure 11 *– Calculation of correlation coefficients within Excel®.*

The particle energy spectral data is also compatible with the Excel® spreadsheet format and consists of 256 discrete energy bins each possessing a 16-bit wide impact counter. The spectrum can be graphed within Excel® for quick viewing and analysis *(figure 12)*.

	A	B
1	Energy Bin (nj)	Count
2	0.00E+00	0.00E+00
3	6.68E+00	5.37E+03
4	1.34E+01	8.97E+03
5	2.00E+01	4.48E+03
6	2.67E+01	1.20E+04
7	3.34E+01	9.06E+03
8	4.01E+01	5.40E+03
9	4.68E+01	6.51E+03
10	5.34E+01	6.12E+03
11	6.01E+01	5.01E+03
12	6.68E+01	4.10E+03
13	7.35E+01	3.58E+03
14	8.02E+01	3.34E+03
15	8.68E+01	3.04E+03
16	9.35E+01	2.79E+03

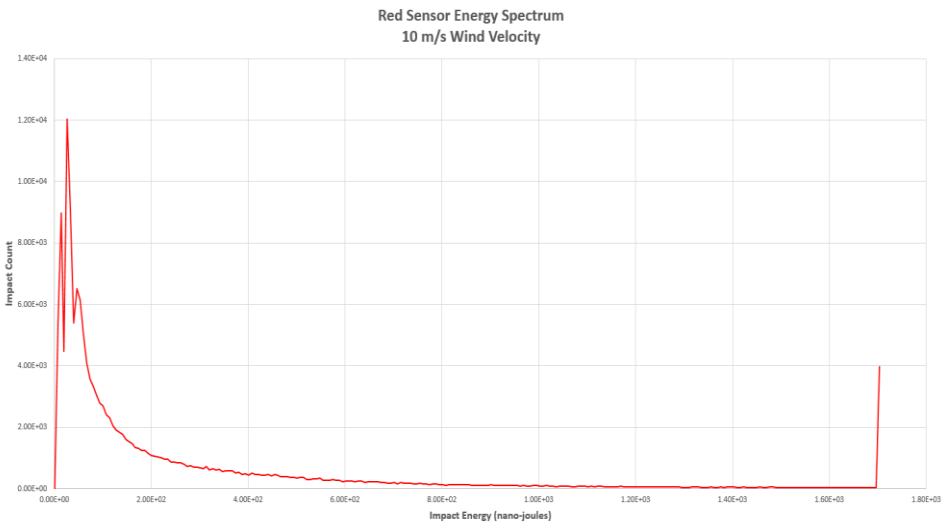

Figure 12 *– Energy spectral data and graph within Excel®.*

Testing and Calibration

The operational requirements for the saltation sensor are defined in *table 1*. There are instrument measurement components within the requirements that address operational range and accuracy. There also are environmental components within the requirements which address the operation and survivability at various atmospheric wind speeds, pressures and temperatures. Lastly, there are system components within the requirements that address instrument compatibility and communication.

SALT.1	The SALT shall measure Martian surface particle flux ranging from 0 to 200 particles/mm^2 s with uncertainty of 10%.
SALT.2	The SALT shall measure the kinetic energy of Martian surface impactors (10 µm < d < 1 mm; 0.5 m/s < v < 20 m/s) with uncertainty of 10%.
SALT.3	The SALT measurement uncertainty shall not change when exposed to Mars surface wind ranging from 0 to 15 m/s.
SALT.4	The SALT shall be capable of capturing measurements at 1 Hz for 1 Martian sol.
SALT.5	The SALT shall be capable of operating with any combination of other MAHRS instruments.
SALT.6.1	SALT equipment that is internally mounted in a rover shall be compatible with a non operating environment of <10^{-5} Torr of $C0_2$ pressure over a temperature range of -40°C to +50°C.
SALT.6.2	SALT equipment that is externally mounted onto a rover shall be compatible with a non operating environment of <10^{-5} Torr of $C0_2$ pressure over a temperature range of -128°C to +50°C.
SALT.7.1	SALT equipment that is internally mounted in a rover shall operate without failure or degradation while exposed to <10^{-5} Torr of $C0_2$ pressure over a mounting interface temperature range of -40°C to +50°C.
SALT.7.2	SALT equipment that is externally mounted to a rover, but not in contact with the Martian surface/soil, shall operate without failure or degradation while exposed to <10^{-5} Torr of $C0_2$ pressure over a mounting interface temperature range of -40°C to +50°C.
SALT.13	The SALT shall be compatible with an operating pressure environment ranging from 0.26 to 1.60 kPa of $C0_2$.
SALT.24	The SALT shall be compatible with an RS-422 command and data interface.

Table 1 *- SALT sensor requirements.*

In order to meet the instrument measurement requirements for the saltation sensor (SALT.1 – SALT.3), a few requisite test apparatuses are needed to calibrate and test the saltation sensor during operation. Firstly, a controlled method for dispensing calibrated particles of known mass and volume and a method to measure the particle rate-of-mass-change per unit area (flux rate) is required to satisfy SALT.1. Secondly, in addition to the requirements imposed on the test apparatus by SALT.1, a method to accurately control the kinetic energy of the particles impacting the saltation sensor must be implemented to satisfy the requirements in SALT.2. Lastly, a method to subject the saltation sensor to wind conditions both with and without particle flow is vital to satisfy the requirements in SALT.3. A sand flume apparatus with two configurations was produced to address the testing requirements of SALT.1 and SALT.2. In order to make the most of the test equipment, the two sand flume apparatuses were produced from the wind tunnel apparatus created to satisfy the testing requirements of SALT.3.

Test Beads

All three configurations of the test apparatus require particles of known mass and volume. In order to meet this requirement, two sources of calibrated particles were acquired and processed to yield suitable test specimens. The first source of calibrated particles was the Potters Class-C Ballotini®Metal Finishing Glass Beads which are described in *table 2*. The density of the glass used to form the beads is approximately 2.45 g/ml.

Designation	US Sieve	Max Diameter (µm)	Min Diameter (µm)	Min % Round	Max Volume (cc)	Max Mass (g)	Min Volume (cc)	Min Mass (g)
C	40-60	425	300 **	75	4.019E-05	9.847-05	1.414E-05	3.464-05

Table 2 *- Potters Class-C Ballotini®Metal Finishing Glass Bead Specifications (**NOTE – Additional sieving moved the lower bound of the bead diameters from 250µm to 300µm).*

The second source of calibrated particles was the Cospheric SSMMS-7.8 Stainless-Steel Metal Microspheres which are described in *table 3*. The density of the stainless-steel used to form the beads is approximately 7.791 g/ml.

Max Diameter (µm)	Min Diameter (µm)	Min % Round	Max Volume (cc)	Max Mass (g)	Min Volume (cc)	Min Mass (g)
425**	360	90	4.019E-05	3.131E-04	2.443E-06	1.903E-04

Table 3 *- Cospheric SSMMS-7.8 Stainless-Steel Metal Microsphere Specifications (**NOTE – Additional sieving moved the upper bound of the bead diameters from 445µm to 425µm).*

Additional sieving (figure 13) was used on both particle sources to tighten the range of diameters of the particles in each sample set. The actual distribution of the particle sizes in each set was not known, but after observation of the beads using a magnifier and a 1951 USAF target *(figures 14a, 14b)*, it was determined that a majority of the bead diameters settled near the 425 µm sieve size. The 1951 USAF target line width is given by *equation 2* below which is also the width of 2.5 line-space pairs *(Glynn, 2010)*.

$$line\,width = \frac{2.5}{2^{\left[group + \left(\frac{element-1}{6}\right)\right]}}$$

Equation 2– *Calculation of 1951 USAF target line-space pair width*

Most of the bead diameters fall between the group 2, elements 4 & 5 (0.442mm – 0.394mm) line widths. Consequently, the upper bound for the bead diameter (425 µm) was used as the standard during testing.

Figure 13 *– 40 & 50 Standard Sieves used on particle sample sets.*

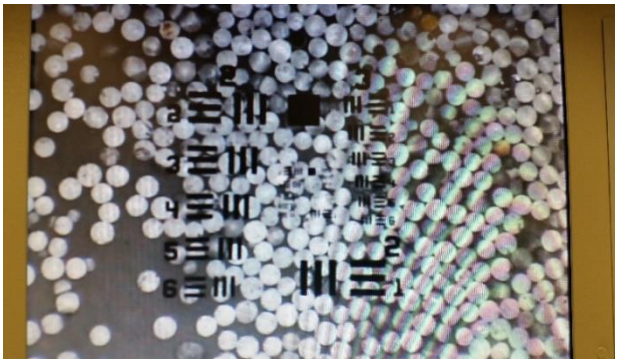

Figure 14a – *Glass bead diameters fall between the widths of lines in group 2, elements 4 & 5 which are approximately 0.442 mm –0.394mm.*

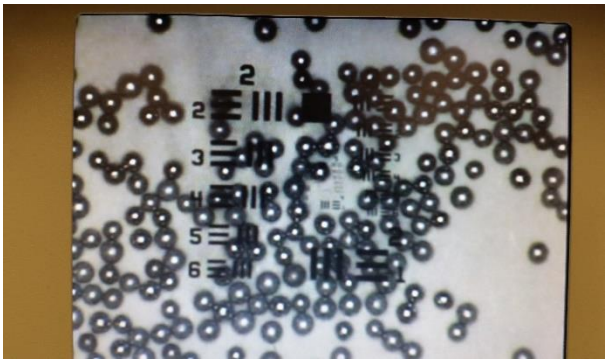

Figure 14b – *Stainless-steel bead diameters fall between the widths of lines in group 2, elements 4 & 5 which are approximately 0.442 mm –0.394mm.*

Sand Flume – 1st Configuration

A sand flume was constructed in order to confirm that the particle flux rate of the beads dispensed as measured by the electronic scale matches the particle flux rate of the impacts measured by the saltation sensor *(figure 15)(Baas, 2003)*. The flume provided accurate metering of beads from a custom designed dispersal mechanism and adequate real-time mass measurement from the electronic scale. The cross-sectional areas of the flume and the sensor are also known to within a reasonable tolerance. The sand dispenser consisted of a funnel shaped reservoir which guided the beads into a nozzle where controlled bursts of air from a compressor and an electronic valve blasted the beads at precise intervals through a series of three cross oriented #40 mesh screens *(figure 16)* that evenly dispersed the beads within the flume cross-section. Further downstream was another set of #40 mesh screens that were adjustable in height from the saltation sensor face *(figures 17a, 17b)*. The outer ring of the adjustable disperser is magnetically coupled to its inner ring. This allowed for varied height drops of the beads, thereby controlling the kinetic energy of the beads prior to impacting the saltation sensor.

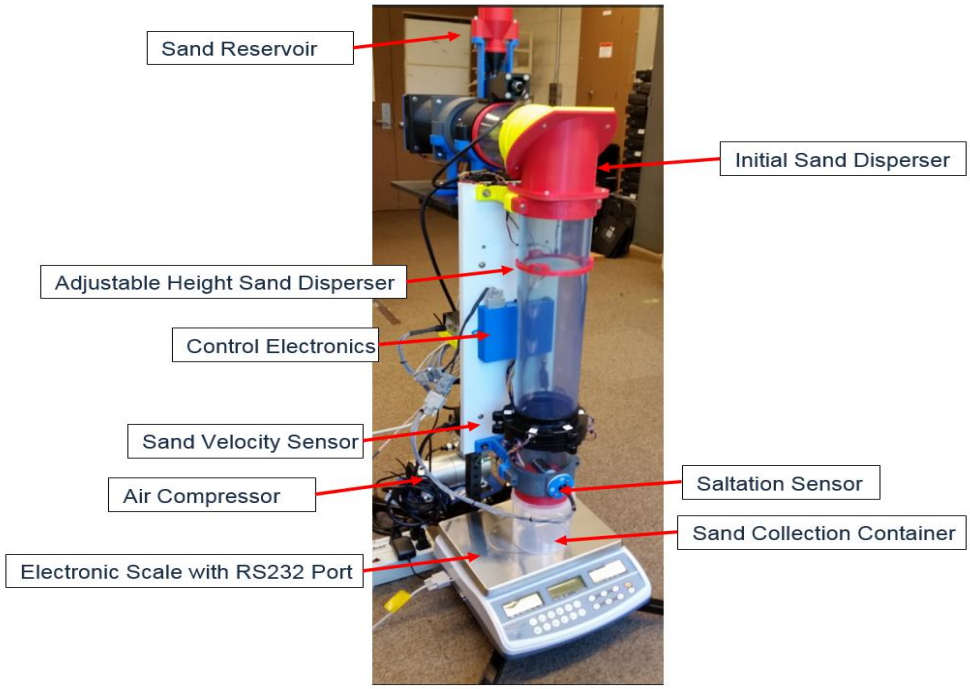

Figure 15 – *First version of sand flume which was used to test the particle flux and energy measurements of the saltation sensor.*

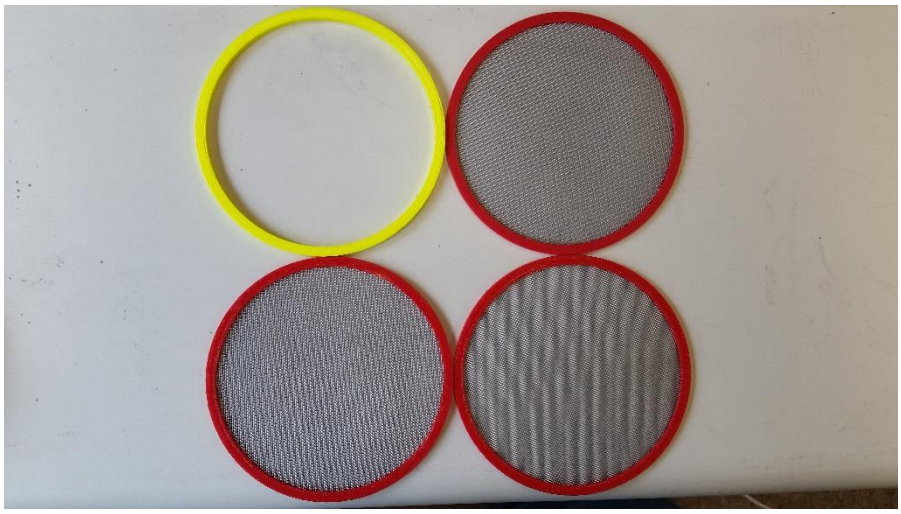

Figure 16 *– The series of three #40 mesh screens contained within the initial sand disperser.*

Figure 17a *– Side view of magnetically-coupled, adjustable-height sand disperser.*

Figure 17b *– Top view of magnetically-coupled, adjustable-height sand disperser.*

Just prior to the saltation sensor is a custom, time-of-flight velocity sensor that measures the bead velocities to within 0.2 m/sec as they are periodically pulsed through the flume tube cross-section. Lastly, an Intelligent® IDC-12 series counting scale measures the mass of the particles dispersed in real-time to within 0.1 gram *(Intelligent® Weighing Technology., 2009)*. The technical specifications of the scale are shown in *table 4*.

Model	**IDC-12**
Maximum Capacity	6000 g
Readability	0.1 g
Tare Range	-6 kg
Repeatability (Std Dev)	0.1 g
Linearity ±	0.2 g
Units of Measure	lb, kg

Table 4 *– IDC-12 Scale Specifications.*

The cross-sectional area of the sand flume is determined by the open cross-sectional area of the velocity sensor because has the most confined area prior to the saltation sensor. Consequently, the flume cross-sectional area is calculated as shown in *figure 18*.

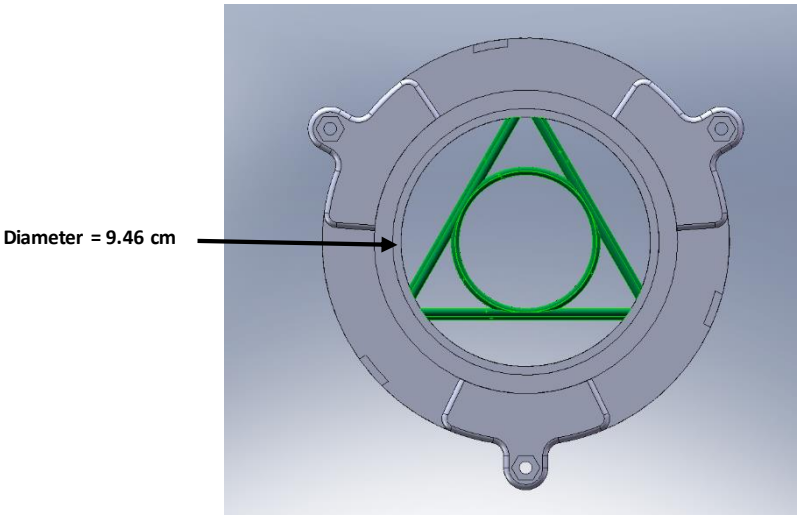

Figure 18 *– The cross-sectional area of the flume is 49.34 cm² which is derived from the 9.46 cm outer diameter yielding an area of 70.29 cm² minus the 20.95 cm² area of green-shaded region.*

During the experiment, two methods of determining the sensor flux were used and compared. The first method used the cross-section of a single quadrant of the sensor. This method used the chord of the exposed region of the aluminum plate times the length of the plate to determine the sensor cross-section (quadrant cross-section = ℓc = 8.35 cm²) *(figures 19a, 19b)*. Using this method, only the impacts on the face of the sensor pointing toward the direction of particle flow were tallied when determining the sensor flux. Unfortunately, this method proved to be sensitive to the angular orientation of the sensor's normal line to the particle flow vector because slight variations in this angle made significant changes in the cross-sectional area of the sensor face. In order to make the sensor more rotationally invariant during testing, a second method using the full cross-section of the sensor, less the area of the gaps between the aluminum plates was employed (full cross-section = $\ell(d - 2g)$ = 11.64 cm²) (Figure 19a, 11b). This method tallied the impacts on the face of the sensor pointing toward the direction of particle flow as well as the impacts on the two adjacent faces of the sensor. Using this method made the sensor less sensitive to its rotational orientation in the particle flow. During the flux calibration test, the saltation sensor records the number of particle impacts per unit time which when divided by the

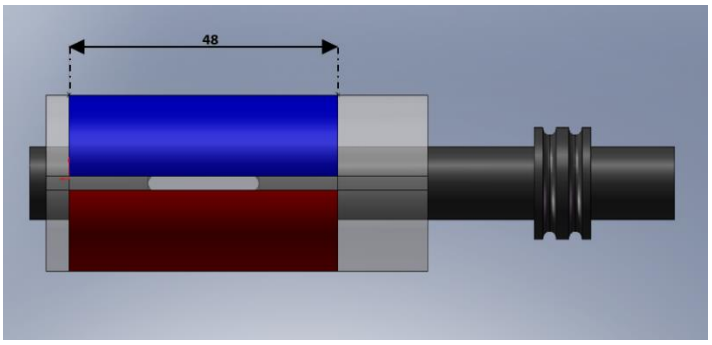

Figure 19a *– Side view of saltation sensor showing length* ℓ ***= 48mm.***

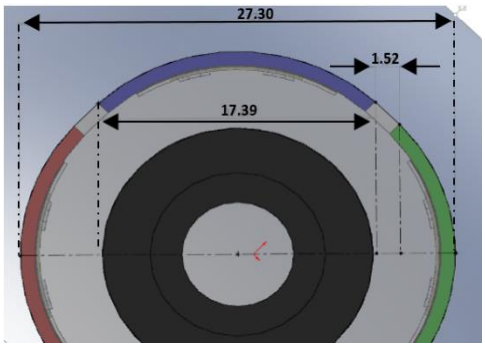

Figure 19b *– Top view of saltation sensor showing quadrant chord* c ***= 17.39mm****, diameter* d ***= 27.3mm,*** *gap width* g ***= 1.52mm.***

sensor cross-sectional area yields the sensor flux as shown in the following expression (***sensor flux = # of sensor impacts/s mm²***). The particle mass-vs-time (***grams/s***) as measured by the electronic scale is divided by the mass of a single particle *(tables 2 and 3)* which is then divided by the flume cross-sectional area yielding the flume flux (***flume flux = # of scale impacts/s mm²***). The resulting data from the flux test runs are shown in *figures 20 - 23*. All of the test plots shown are the result of 20,000 to 30,000 particle impacts upon the saltation sensor.

Figure 20 *– Blue quadrant sensor flux test.*

As shown in the flux graphs for the blue quadrant *(figure 20)*, using the method that makes use of the full cross-section of the sensor improves the match between the flux as measured by the scale (brown line) and the composite flux using the blue quadrant and adjacent quadrants (gray line) as compared to the single blue quadrant flux (blue line). Nevertheless, all of the blue quadrant results fall outside of the 10% allowable deviation. Clogging of the dispersion mesh was thought to be the most likely cause for the large deviation. This clogging usually starts with the outer regions of the mesh, thereby concentrating the flow toward the center of the flume, increasing the particle flux across the sensor and also invalidating the presumed cross-sectional area of the flume. However, on rarer occasions, the center region of the mesh would clog and reduce the particle flux across the sensor which also invalidated the presumed cross-sectional area of the flume.

As seen previously with the blue quadrant flux test, the yellow quadrant flux test has one result with a clogged dispersion mesh and one with a clean dispersion mesh *(figure 21)*. The favorable result shows the sensor flux and scale flux readings within the 10% error band (deviation shown in gray for the 38cm drop was calculated to be 9.14%).

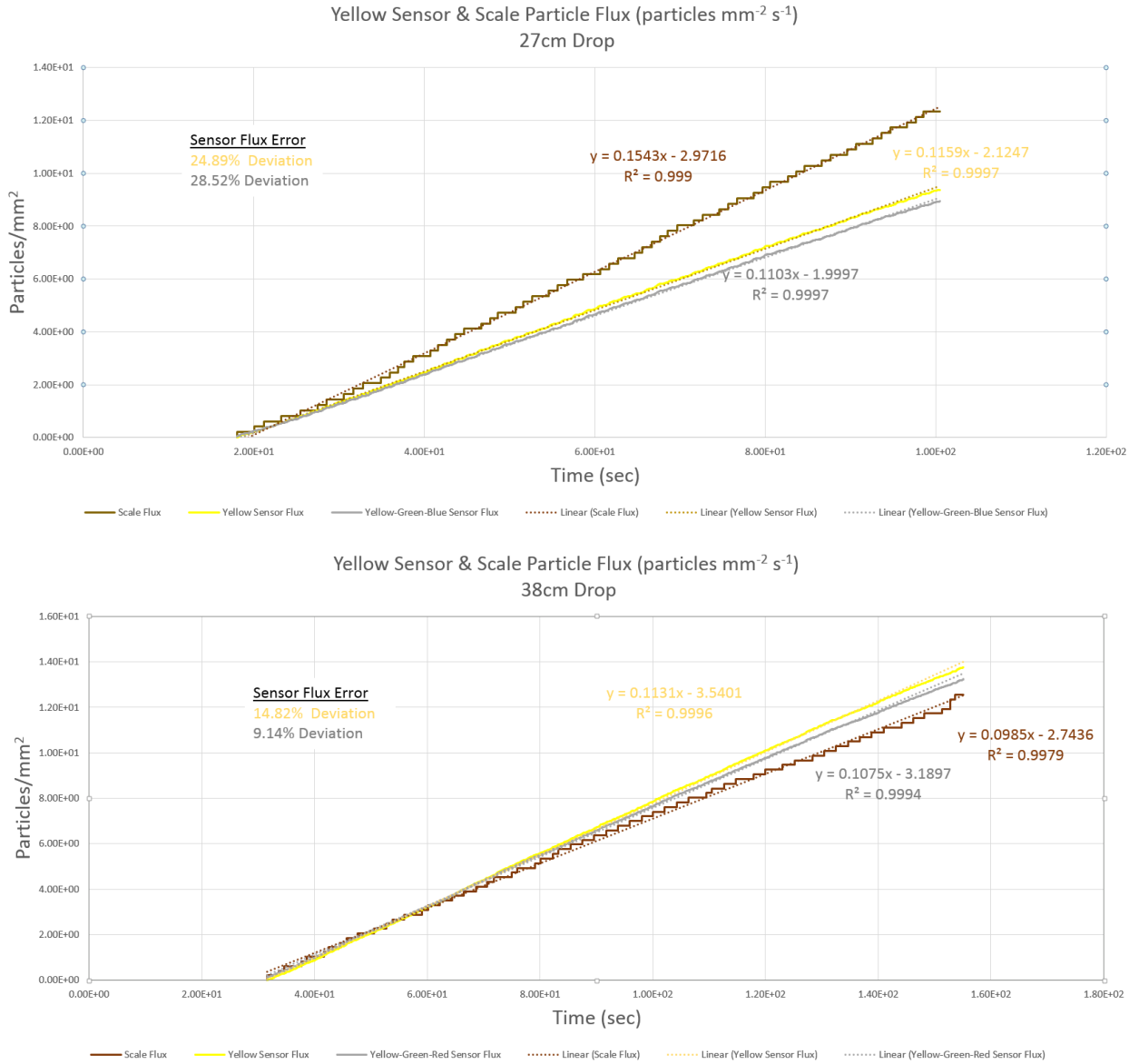

Figure 21 *– Yellow quadrant sensor flux test.*

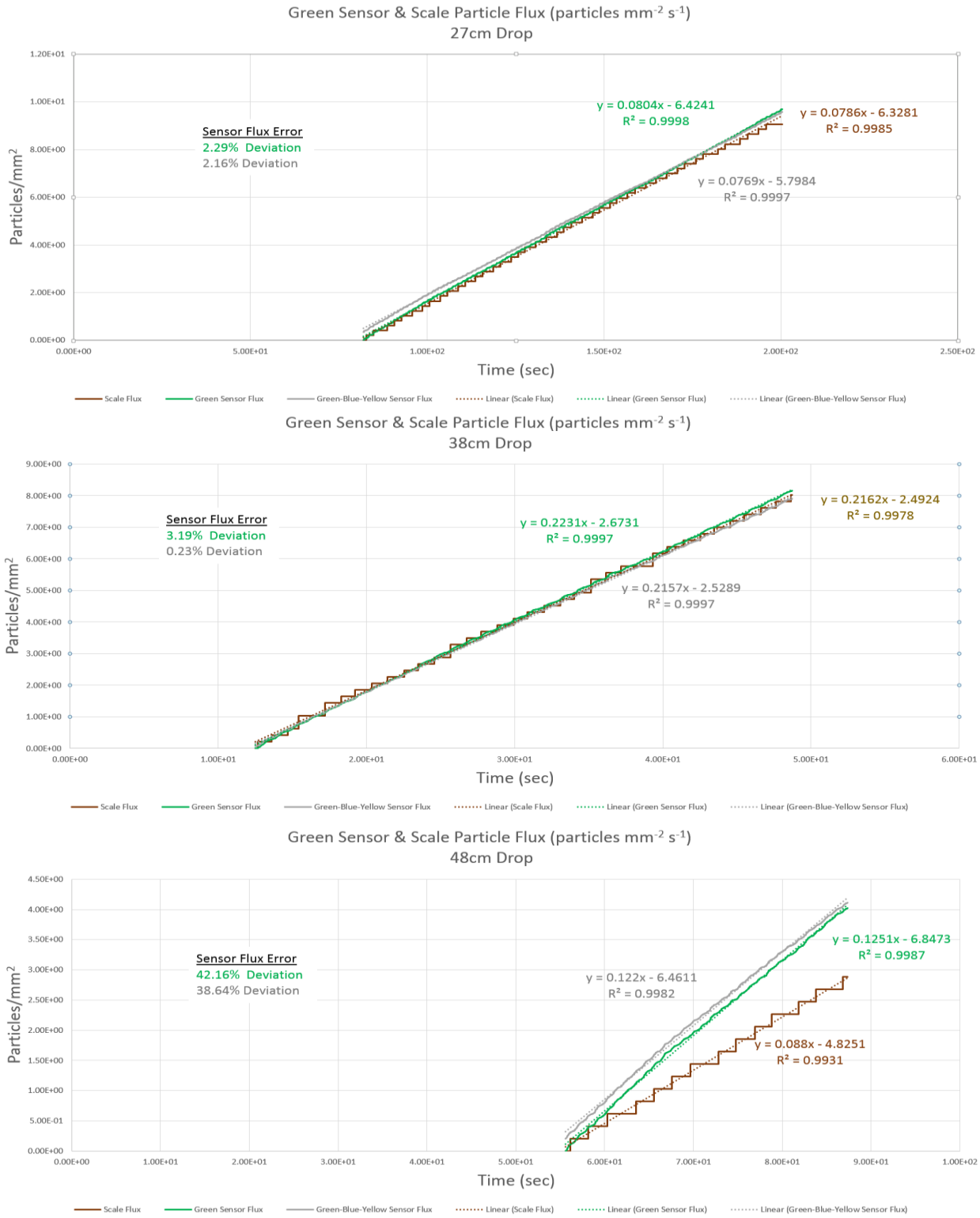

Figure 22 *– Green quadrant sensor flux test.*

The 27cm and 38cm particle drops for the green quadrant flux test show excellent agreement between the sensor and scale flux measurements with 2.16% and 0.23% deviations *(figure 22)*. Even the individual quadrant flux measurements (green lines) showed excellent agreement with 2.29% and 3.19% deviations from the scale flux measurements. This indicates that the sensor orientation in the flume was close to ideal. The last flux test suffered from clogged dispersion meshes as in previous test runs.

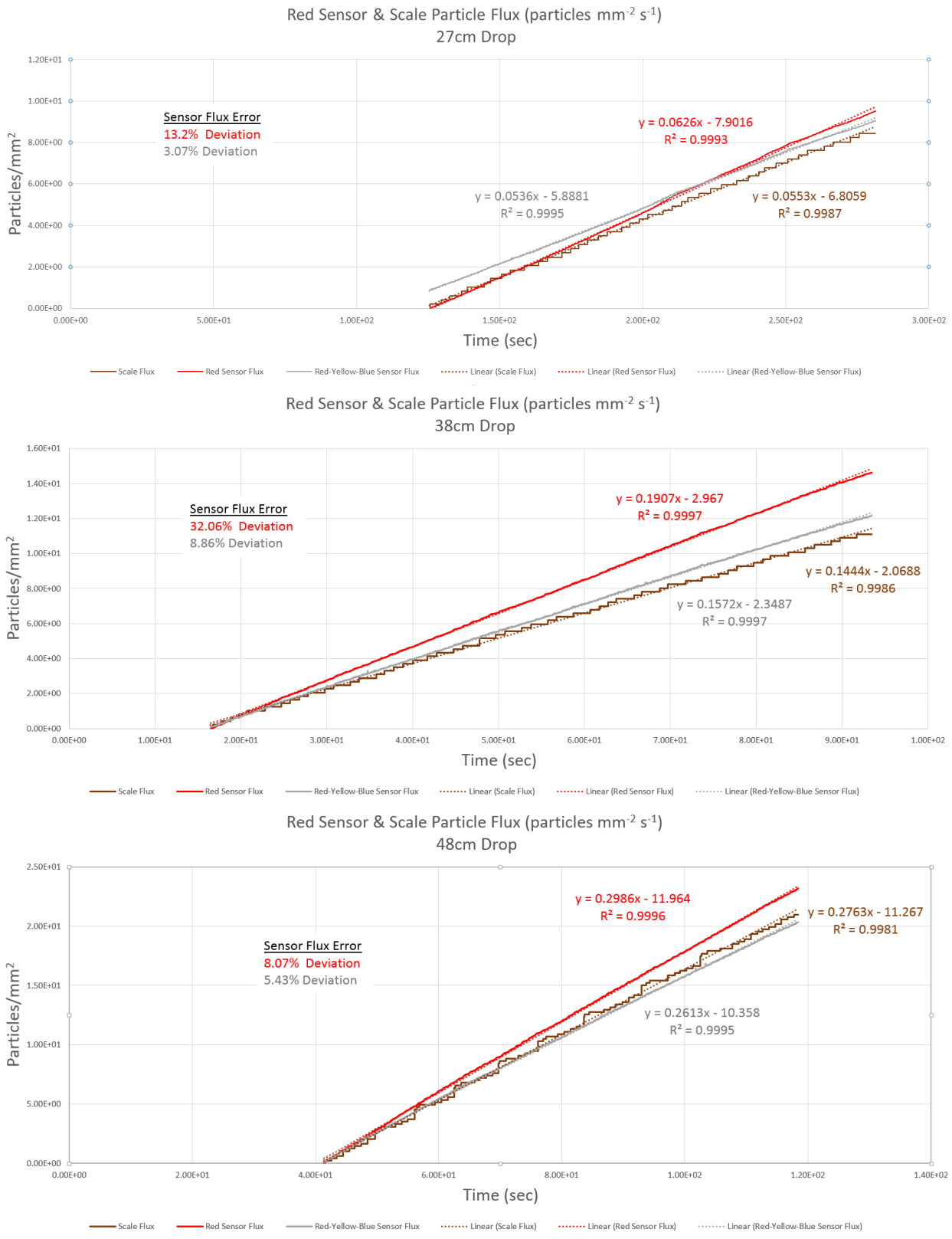

Figure 23 *– Red quadrant sensor flux test.*

All three of the red quadrant flux tests showed good agreement between the full-sensor flux and scale flux measurements with deviations of 3.07%, 8.86% and 5.43% *(figure 23)*.

Sand Flume Flux Test Results

As seen by the results in *figures 20 – 23*, a problem was discovered during testing that was the result of the clogging of the disperser screens. As a number of sequential tests were performed, the screens would gradually clog, creating an uneven distribution of particles within the flume tube and invalidating the calculated cross-sectional area of the flume tube. Ideally, the screens should have been cleaned between each test, but the problem was not fully understood until testing was completed and the data analyzed. Better results were observed in the data sets that proceeded a cleaning of the screens. Nevertheless, it was demonstrated that results within the 10% error margin between the sensor and scale flux measurements could be obtained if vigilant about maintaining clean disperser screens proceeding each test. The requirements stipulated in SALT.1 have been mostly satisfied with the exception of the flux rate. The sand flume apparatus in its current configuration lacks the ability to generate a controlled high flow dispersal of particles. However, it was demonstrated that good agreement between the measured flume and sensor flux rates can be obtained.

Sand Flume – 2nd Configuration

The height adjustment mechanism in the first configuration of the sand flume proved to be problematic. The beads would statically stick to the inner walls of the flume tube and prevent the movement of the adjustable disperser. Consequently, a second version of the sand flume was created that made reliable, easy height adjustment the main priority *(figure 24)*. This adaptation of the sand flume was a miniaturized version of the original particle disperser with a similar mesh arrangement and vibrator assembly that was designed to slide directly in the flume tube.

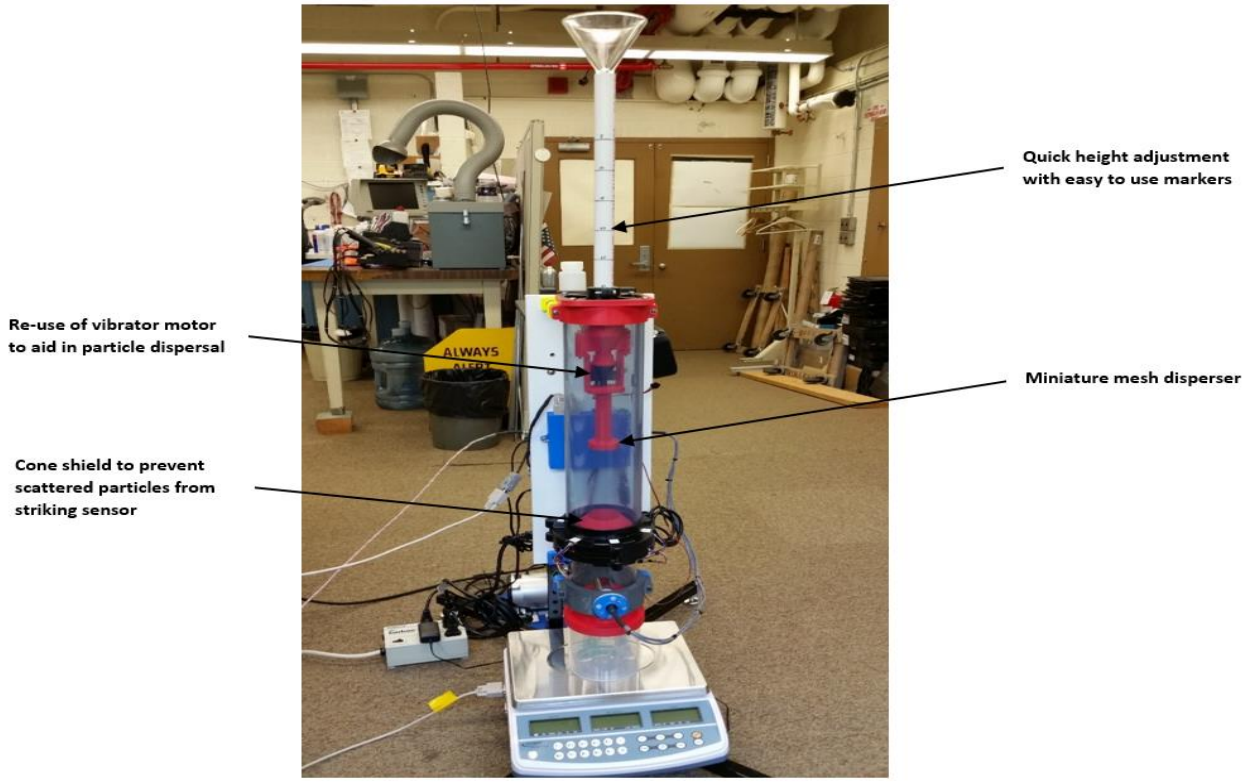

Figure 24 – *Second version of sand flume which was strictly used to calibrate the particle energy measurements of the saltation sensor.*

This particular setup was used to acquire data for the energy calibration of the saltation sensor. The saltation sensor is incapable of measuring the energy levels of individual particle impacts without additional information. This is partially due to the fact that particle trajectory relative to the sensor surface determines the amount of energy transferred during the collision. Therefore, it was understood that the energy measurements required a time averaged measurement of many particle collisions. During flume testing, the sensor was immersed in a constant flow of particles with trajectories that predominately travelled parallel to the gravity vector or normal to the plane tangential to the front face of the sensor surface. This calibrated fluence of particles with known velocity and mass allowed for a global calculation of average particle energy (particle kinetic energy = $mv^2/2$). The first configuration of the flume drop test used the time-of-flight velocity ring to determine the velocity of the particles whereas the later flume drop test used the height of the drop and the air resistance to calculate the particle velocity as shown in *equation 3*.

$$\text{Particle Velocity} = \sqrt{\frac{g}{b}\left(1 - e^{-2bh}\right)} \quad ; \quad b = \frac{1}{2}\frac{\rho}{m}C_D A$$

$g = 9.8\ m/s^2$
$\boldsymbol{\rho}$ = air density = $1.2\ kg/m^3$
m = particle mass = 9.85×10^{-8} kg *(glass beads)*, 3.13×10^{-7} kg *(stainless-steel beads)*
C_D = drag coefficient for sphere = 0.47 *(Wikipedia WebSite, Drag Coefficient)*
A = particle cross-sectional area = $1.42 \times 10^{-7}\ m^2$ *(425 µm bead diameter)*
h = particle height m

***Equation 3**– Calculation of particle velocity in the presence of air resistance (Hyperphysics WebSite - Freefall Velocity vs Distance for Quadratic Drag).*

Sand Flume Energy Test Results

The heavier stainless-steel beads were used in second flume configuration test, in contrast to the previous tests where the lighter glass beads were used throughout the test process. Consequently, the gain setting of the saltation sensor had to be altered from the high setting (x20) to the low setting (x10) because the increased energies from the stainless-steel beads were saturating the saltation sensor. The threshold setting for both the flux testing and energy testing was kept the same (threshold = 100). The reduced cross-sectional area of the miniature disperser covered a smaller portion of the sensor. In contrast, the first configuration of the flume immersed the entire sensor in the particle flow. Nevertheless, just as in the previous flume test, only the primary sensor quadrant impacts were used in the energy calculation. The data from the two flume experiments was then compared by examining how closely the averaged correlation coefficients from each test matched. This was done for both the pulse area and pulse height measurements to see which feature yielded the most consistent coefficient values. The energy and peak coefficients were derived by simply dividing the average particle energies by the average pulse areas and average peak heights. Of course, this assumes the existence of a linear relationship between these quantities. Unfortunately, the data set from the original flume setup produced only three points per quadrant due to the difficulties of the drop-height adjustment. As a result, a linear fit was not performed. Instead, the coefficients derived from each of three selected heights were averaged. The energy data from the first flume configuration using the glass beads is shown in *figure 25* where the average energy coefficient ($1.66823e^{-9}$) and the average peak coefficient ($5.52271\ e^{-9}$) are calculated. The convenient drop height adjustment of the second configuration made it possible to acquire five acceptable points per quadrant *(figure 26)* which made a meaningful linear fit possible.

	Glass Bead Diameter (um)	Glass Bead Density (g/ml)		
	425	2.45		
	Avg Particle Velociy (m/s)	**Avg Particle Energy (Kgm2s-2)**	**Avg Sensor Pulse Energy**	**Avg Sensor Pulse Peak**
Blue - 27cm	1.599324324	1.25943E-07	93.97678019	28.73228116
Blue - 38cm	1.976603774	1.92372E-07	92.17096633	28.52184996
Blue - 48cm	1.979081633	1.92854E-07	128.1072416	36.59492858
Yellow - 27cm	1.640756303	1.32553E-07	77.45914941	25.82452874
Yellow - 38cm	1.694244604	1.41336E-07	94.46810735	30.19841619
Yellow - 48cm	2.206804734	2.39789E-07	101.6932084	31.85704809
Green - 27cm	1.604054054	1.26689E-07	95.05190361	30.24784037
Green - 38cm	2.002040816	1.97355E-07	110.2068687	32.926
Green - 48cm	2.044505495	2.05815E-07	137.5297941	39.42692828
Red - 27cm	1.529444444	1.15178E-07	99.9937727	29.30661352
Red - 38cm	1.842857143	1.67219E-07	109.656182	31.57820667
Red - 48cm	2.258080808	2.51062E-07	112.8962606	31.75391797
	Pulse Energy Coefficient	**Pulse Peak Coefficient**		
Blue - 27cm	1.34015E-09	4.38333E-09		
Blue - 38cm	2.08712E-09	6.74471E-09		
Blue - 48cm	1.50541E-09	5.26997E-09		
Yellow - 27cm	1.71126E-09	5.13283E-09		
Yellow - 38cm	1.49613E-09	4.68026E-09		
Yellow - 48cm	2.35797E-09	7.52703E-09		
Green - 27cm	1.33284E-09	4.18837E-09		
Green - 38cm	1.79077E-09	5.99388E-09		
Green - 48cm	1.49652E-09	5.22018E-09		
Red - 27cm	1.15185E-09	3.9301E-09		
Red - 38cm	1.52494E-09	5.29538E-09		
Red - 48cm	2.22383E-09	7.90648E-09		
	Avg Energy Coeffecient	**Avg Peak Coefficient**		
	1.66823E-09	5.52271E-09		

Figure 25 *– Raw data from the energy test using the glass beads;* $Coefficient_{PulseEnergy}$ *= Particle Energy/Pulse Energy*
$Coefficient_{PulsePeak}$ *= Particle Energy/Pulse Peak*

It should be noted that sixth point in each of the graphs was omitted because in each case the 30 cm drop height resulted in data suggesting an energy level lower than the 25 cm drop height. Increased particle scattering off of the inner flume surfaces is most likely the explanation for this anomaly. The sensor energy (pulse area) and sensor height (pulse peak) were plotted vs the particle energy and a linear fit whose slope represented the inverse of the corresponding energy and pulse coefficients was calculated *(figures 27, 28)*. The correlation coefficient of the linear fit was then used to verify the "goodness of fit" between these quantities.

Blue

Drop Height (cm)	Avg Particle Velociy (m/s)	Avg Particle Energy (Kgm2s-2)	Avg Sensor Pulse Energy	Avg Sensor Pulse Peak
5	0.9867957	1.5247E-07	242.9565868	59.73729864
10	1.391103	3.03003E-07	403.0977881	72.79182879
15	1.698342	4.51626E-07	573.9100877	101.2430684
20	1.954869	5.98362E-07	681.5986667	86.86187845
25	2.178706	7.43235E-07	1413.671608	170.5992403
30	2.379131	8.86269E-07	1097.238519	117.9876999

Yellow

Drop Height (cm)	Avg Particle Velociy (m/s)	Avg Particle Energy (Kgm2s-2)	Avg Sensor Pulse Energy	Avg Sensor Pulse Peak
5	0.9867957	1.5247E-07	272.6698337	67.44810379
10	1.391103	3.03003E-07	431.3107511	86.7342233
15	1.698342	4.51626E-07	428.0595948	83.68904245
20	1.954869	5.98362E-07	766.0509259	129.5235669
25	2.178706	7.43235E-07	687.0686275	114.0122075
30	2.379131	8.86269E-07	803.546735	118.0725552

Green

Drop Height (cm)	Avg Particle Velociy (m/s)	Avg Particle Energy (Kgm2s-2)	Avg Sensor Pulse Energy	Avg Sensor Pulse Peak
5	0.9867957	1.5247E-07	425.3362702	89.44053398
10	1.391103	3.03003E-07	564.5226277	96.45978391
15	1.698342	4.51626E-07	871.6066176	125.9389002
20	1.954869	5.98362E-07	805.3044059	105.8641425
25	2.178706	7.43235E-07	1058.859397	118.2407628
30	2.379131	8.86269E-07	834.7957393	114.0997899

Red

Drop Height (cm)	Avg Particle Velociy (m/s)	Avg Particle Energy (Kgm2s-2)	Avg Sensor Pulse Energy	Avg Sensor Pulse Peak
5	0.9867957	1.5247E-07	234.5355893	56.51714006
10	1.391103	3.03003E-07	514.4668471	98.03370787
15	1.698342	4.51626E-07	651.5087483	108.6708005
20	1.954869	5.98362E-07	761.2066474	108.1293833
25	2.178706	7.43235E-07	982.177624	140.4975657
30	2.379131	8.86269E-07	898.2962085	118.6765286

Figure 26 *- Raw data from the energy test using the stainless-steel beads. The 30 cm drop height (highlighted in yellow) was consistently problematic (always smaller signal than lower height).*

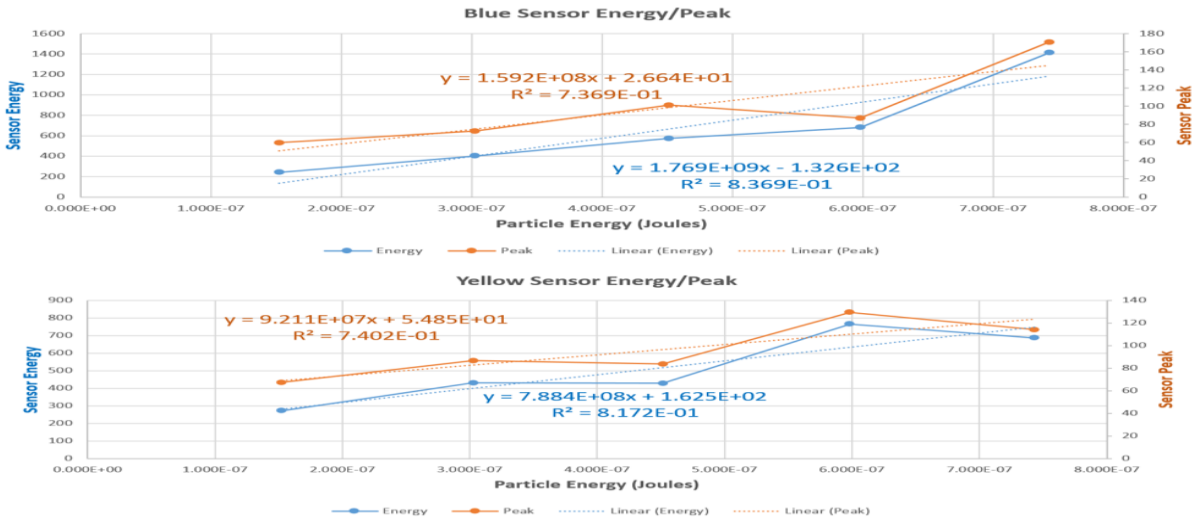

Figure 27 *– Particle Energy vs Blue-Yellow Sensor Energy & Sensor Peak using stainless-steel beads.*

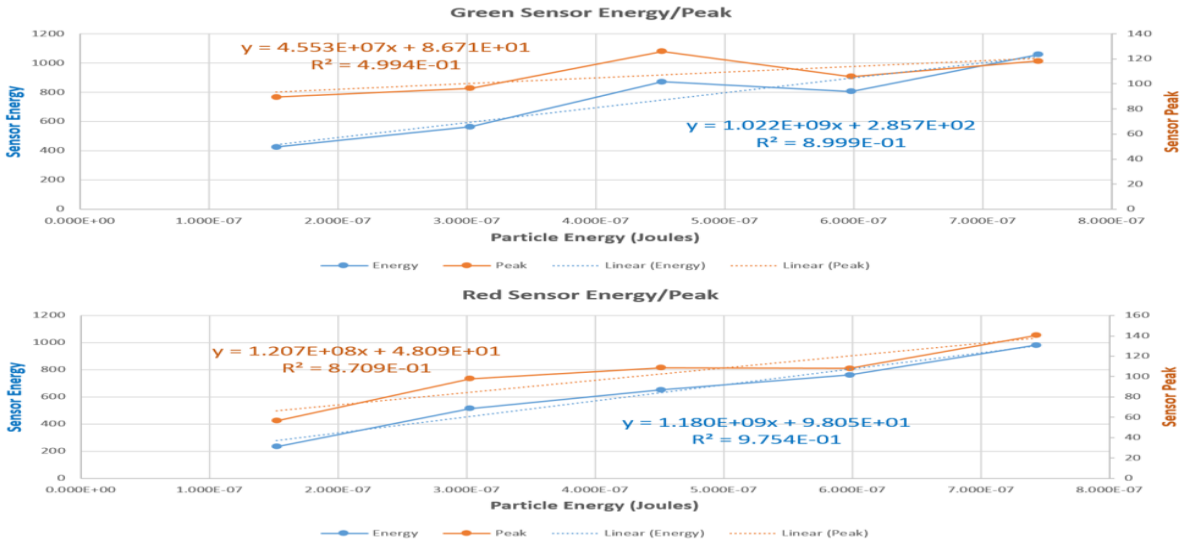

Figure 28 *– Particle Energy vs Green-Red Sensor Energy & Sensor Peak using stainless-steel beads.*

Observing the correlation coefficients (R^2) in *figures 27 and 28*, shows that in all circumstances the sensor energy (pulse area) makes a better fit to the particle energy than the sensor peak (pulse height). The coefficients are the inverse of the slopes from the graphs multiplied by two. The energy coefficient derived from the sand flume test ($c_{FlumeSand}$) is equivalent to the averaged particle energy ($\bar{E}_{ParticleFlumeSand}$) divided by averaged pulse area of the saltation sensor ($\bar{E}_{PulseAreaFlumeSand}$) times the gain factor (g_{sand}) of the signal processing amplifier stage. The gain factor used during the sand flume testing (g_{Sand}=20) was double that of the gain factor used during stainless-steel flume testing ($g_{StainlessSteel}$=10). All tests results are calculated relative to the initial sand tests by fixing g_{Sand} to unity. Therefore, a scale factor of two is required to correctly calculate the energy coefficient derived from the stainless-steel flume test ($c_{FlumeStainlessSteel}$) as seen in equation 4.

$$c_{FlumeSand} = \frac{\bar{E}_{ParticleFlumeSand}}{g_{Sand}\bar{E}_{PulseAreaFlumeSand}}; \quad \text{where } g_{StainlessSteel} = \frac{g_{sand}}{2}$$

$$c_{FlumeStainlessSteel} = \frac{\bar{E}_{ParticleFlumeStainlessSteel}}{g_{StainlessSteel}\bar{E}_{PulseAreaStainlessSteel}} = \frac{2\bar{E}_{ParticleFlumeStainlessSteel}}{g_{Sand}\bar{E}_{PulseAreaStainlessSteel}}$$

Equation 4 *– Calculation of correlation coefficients with gain considerations.*

The data from the graphs is displayed in tabular form *(figure 29)* and the coefficients are calculated and averaged to establish global values relating the particle energy to the sensor pulse area and peak.

Afterward, the coefficients established from the glass bead tests and the stainless-steel bead tests were averaged and their deviations calculated to see which measured quantity correlates best with the particle energy measurements.

	Stainless Bead Diameter (um)	Stainless Bead Density (g/ml)
	425	7.791
	Energy Stats	**Peak Stats**
Blue - Slope	1769190318	159222347.1
R^2	0.836947685	0.73690586
Yellow - Slope	788359442.1	92113147.91
R^2	0.817189134	0.740179483
Green-Slope	1021519602	45534513.92
R^2	0.899937983	0.499430576
Red - Slope	1180089254	120683904.9
R^2	0.975385817	0.870922866
	Avg Energy Coeffecient	**Avg Peak Coefficient**
	1.68097E-09	1.91592E-08

Figure 29 *- Energy test results from the stainless-steel beads;* $c_{PulseEnergy} = 2/Slope_{Energy}$, $c_{PulsePeak} = 2/Slope_{Peak}$
****Note - Coefficients are doubled *(note factor of 2 in numerator)* because the gains are halved in these test runs.**

Note the average energy coefficient ($1.681\,e^{-9}$) and the average peak coefficient ($1.916\,e^{-8}$) from the stainless-steel bead energy test *(figure 29) as compared to t*he average energy coefficient ($1.668\,e^{-9}$) and the average peak coefficient ($5.523\,e^{-8}$) from the glass bead energy test *(figure 25)*. The energy coefficients between the glass bead and stainless-steel bead test runs are within 0.761% of each other. The peak coefficients, on the other hand, deviate by more than 110%. This discrepancy along with the less accurate linear fits, suggests that the pulse peak values are not the best quantity to correlate with the averaged particle energy. In comparison, the pulse area values seem to reasonably correlate with the averaged particle energy. Furthermore, the small deviation between the calculated coefficients, in spite of the two tests using different particle masses, velocity measurement methods and signal gains, suggests that the pulse area is a robust mechanism for inferring the average particle energy impinging on the sensor surface. Averaging the glass and stainless-steel test results yield an energy coefficient of $1.675\,e^{-9}$ which is used hence forth as the de facto energy coefficient for the gravity-drop flume tests. Once again a limitation of the testing apparatus prevents a full test of the requirements detailed in SALT.2 because only velocities up to 3 m/s are achievable. Nevertheless, the possibility of measuring the average particle energy to within 10% looks very promising after running hundreds of thousands of particle impacts with two completely different test setups and deriving two results within 0.761% of each other.

Wind Tunnel Flux Tests

Gravity-drop flume testing provided a simple means to verify the proper operation of the saltation sensor, but wind-sand interaction is a key component of saltation that only field testing *(Sherman, et al. 2011)* or wind-tunnel testing can satisfy. Consequently, a lot of effort went into the design of a wind tunnel capable of measuring particle velocity and particle flux *(figure 30)* while minimizing turbulent flow around the saltation sensor *(figure 31)*. Knowing that a flume drop configuration was also required, the wind tunnel had to be reconfigurable to accommodate both test formations. Unfortunately, the limitations of the testing apparatus (specifically the wind tunnel fan and sand collection apparatus), prevented total fulfillment of the SALT.2 kinetic energy verification which requires wind speeds in excess of 20 m/s. However, the requirements of SALT.3 were partially verified within the wind tunnel because the saltation sensor did not register any impacts solely due to wind (no particle injection) with velocities exceeding 15 m/s.

The sand capture container in conjunction with the electronic scale and the loose coupling mechanism between the wind tunnel and capture container, facilitated the measurement of the particle flux with wind speeds up to 10 m/s. The 10 m/s wind speed limitation was established after it was discovered that wind speeds beyond 10 m/s caused the scale readings to become unstable thereby invalidating the particle flux measurement. This arrangement permitted particle flux testing in more realistic windy operating conditions.

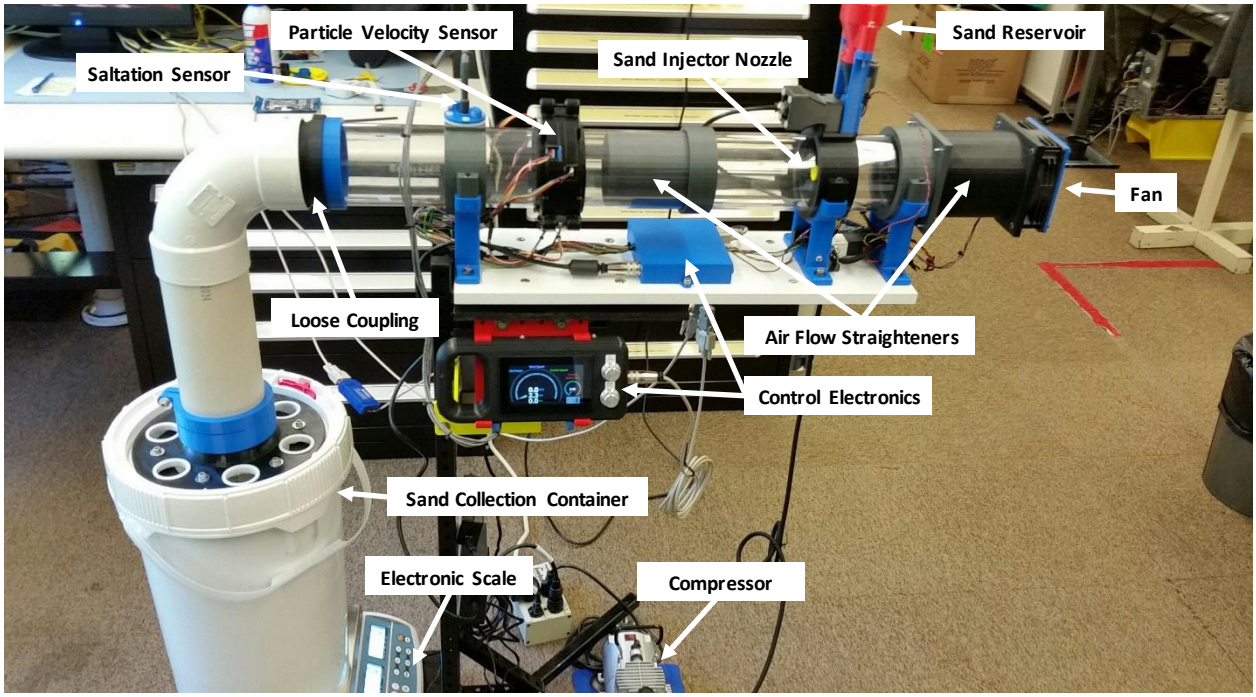

Figure 30 *– Wind tunnel layout.*

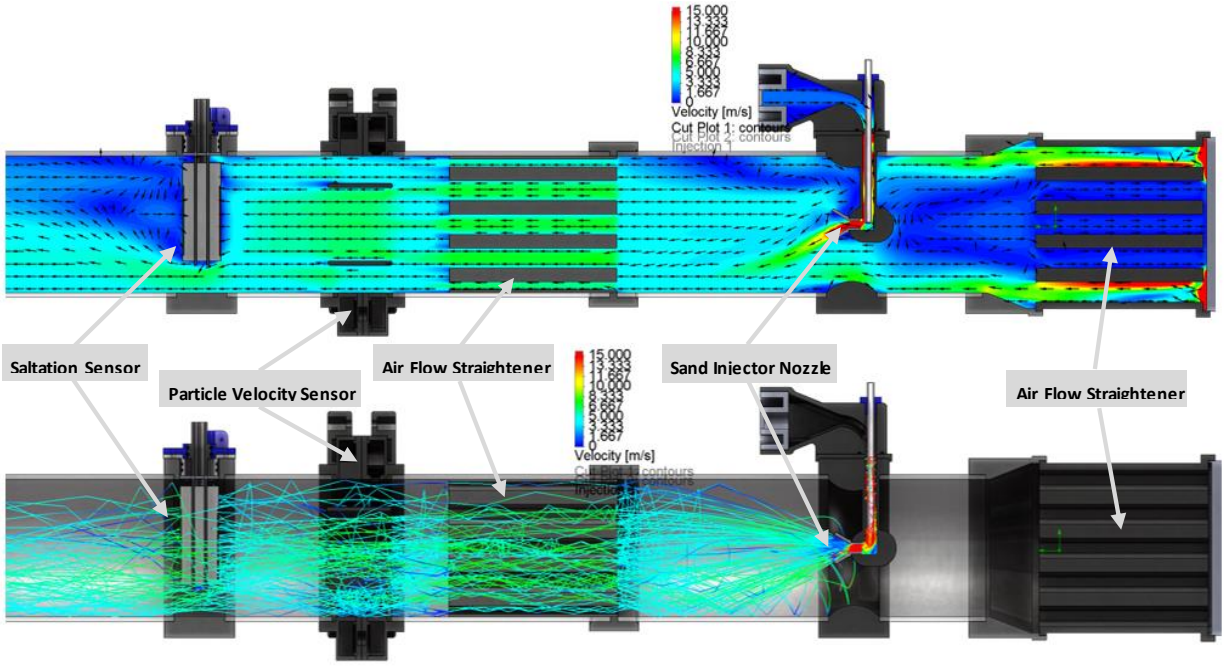

Figure 31 *– Cross-sectional views of the computational flow dynamics analysis performed on the wind tunnel to examine wind turbulence (top view) and particle flight trajectories (bottom view).*

Particle flux testing within the wind tunnel yielded similar results to the corresponding gravity-drop flume tests. More specifically, the flux tests performed on the green, red and yellow quadrants of the saltation sensor all fell within 10% of the scale flux measurements *(figures 32—34)*. The blue sensor quadrant, however, showed substantial deviation in flux from the scale measurement *(figure 35)* as observed in the previous gravity-drop flume tests. After witnessing this anomaly for the second time, a concerted effort was made to balance the gains and offsets between each of the four signal conditioning stages of the saltation sensor quadrants. Nevertheless, the results remained unchanged which suggests that the blue quadrant sensor is more sensitive than the other quadrants. The earlier assertion that disperser screen clogging was the sole source of error between the blue sensor quadrant flux measurements and the scale flux measurements was now proven to be incorrect. Now it seems that the most likely cause for the excessive blue quadrant sensor flux deviations stems from inadequate manufacturing tolerances during the sensor assembly. The variation in the epoxy thickness between the piezo-electric film and the aluminum substrate of each quadrant as well as the variation of the piezo-electric film placement on the aluminum substrate for each quadrant are the manufacturing processes that require tighter control. This would require upgrading many of the jigs that were employed during the manufacturing process to maintain build uniformity.

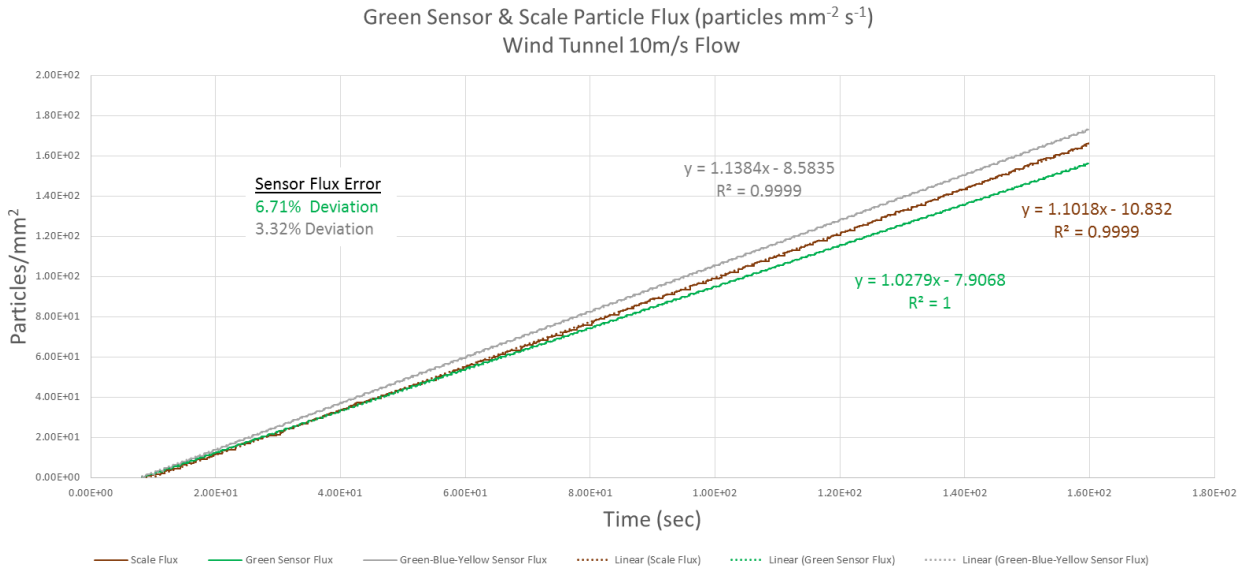

Figure 32 *– Wind tunnel flux test using green sensor quadrant.*

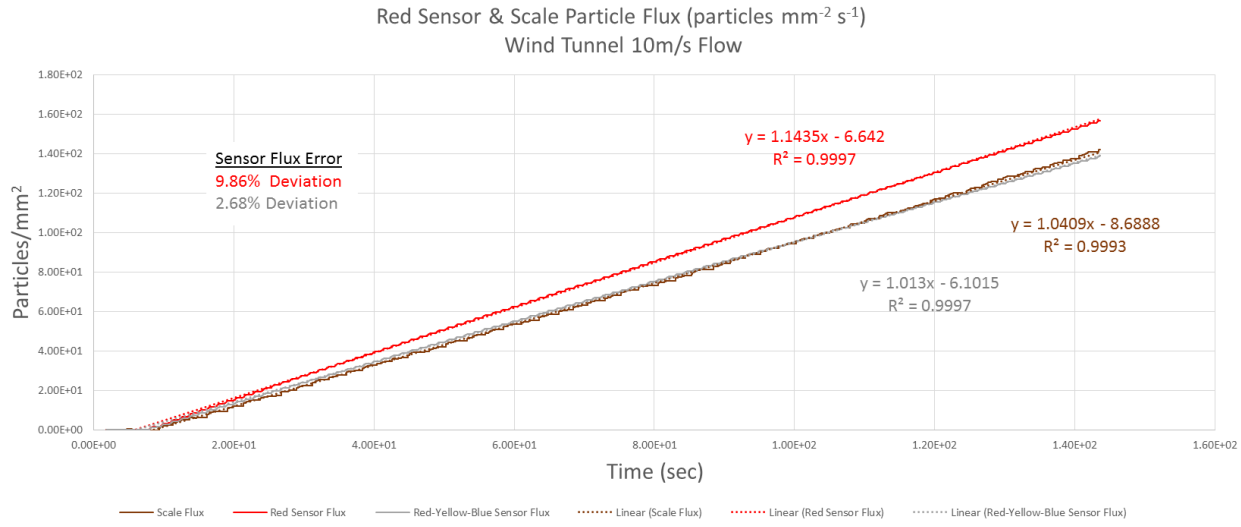

Figure 33 *– Wind tunnel flux test using red sensor quadrant.*

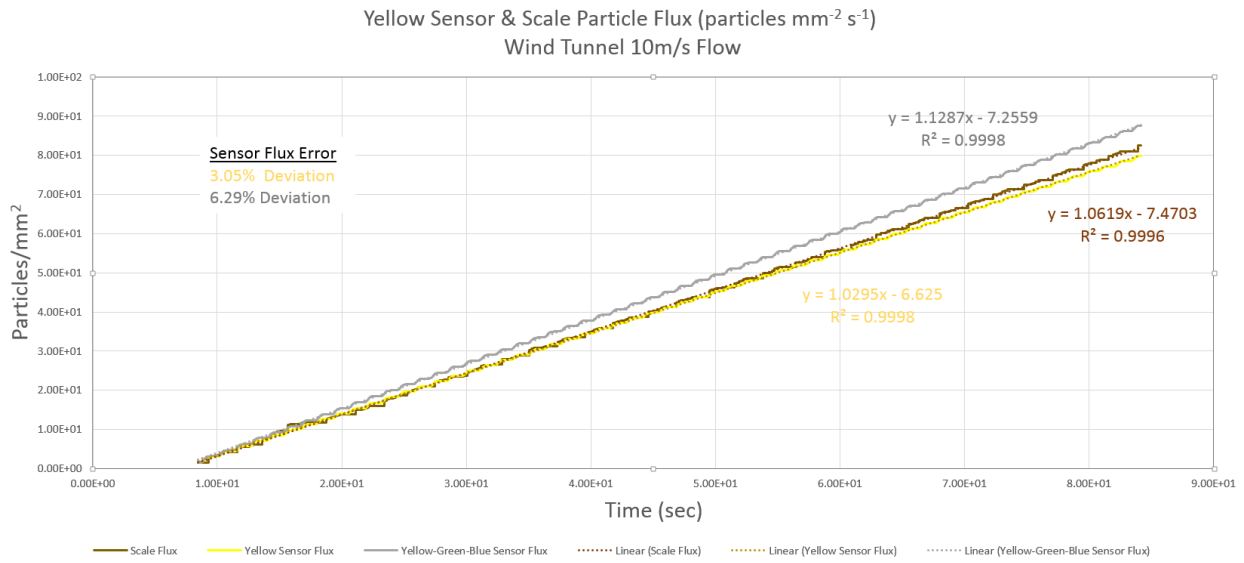

Figure 34 *– Wind tunnel flux test using yellow sensor quadrant.*

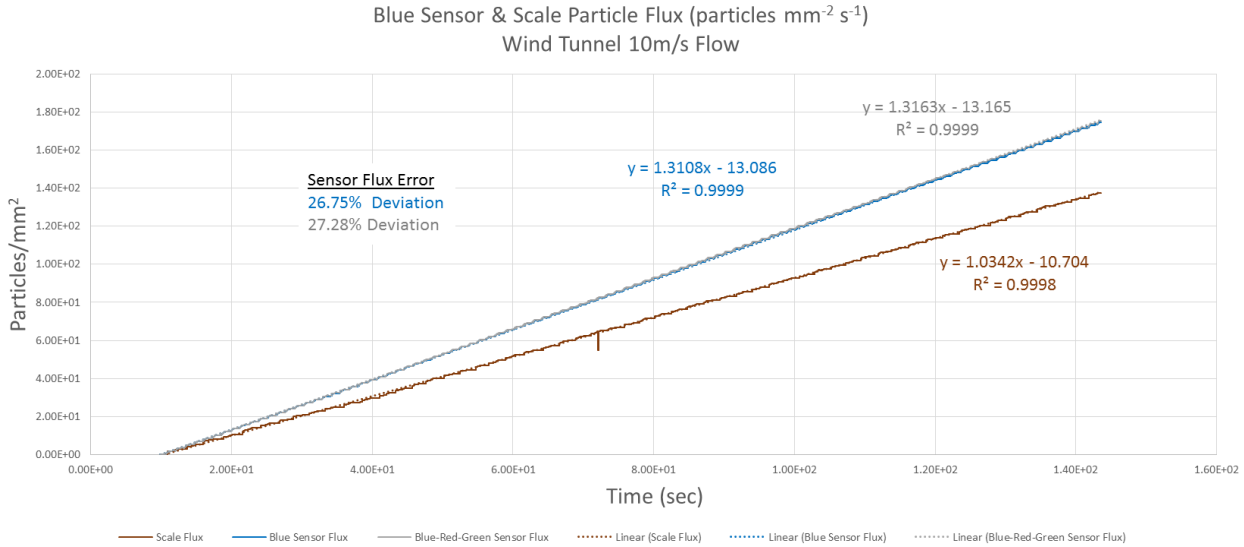

Figure 35 *– Wind tunnel flux test using blue sensor quadrant.*

A more sensitive blue quadrant sensor equates to a lower impact threshold which would cause the saltation sensor to count particle impacts with lower energy levels, thereby increasing the total count. With this is mind, a linear fit of the scale flux and the blue quadrant sensor flux was performed to extract the scale factor between the two measurements and to examine the closeness of fit by studying the correlation coefficient *(equation 5).*

$$Flux_{Scale} = 0.7975\,Flux_{BlueSensorQuadrant} - 2.1491; R^2 = 0.9998$$
$$Flux_{Scale} = 0.8037\,Flux_{BlueRedGreenSensorQuadrants} - 2.2861; R^2 = 0.9997$$

Equation 5*– Calculation of scale factors to correct flux measurement errors.*

The linear fit between the scale flux and the blue quadrant sensor flux is quite good as seen by the corresponding correlation coefficients. Using these scale factors from the wind tunnel data and applying them to the blue quadrant gravity-drop flume test data shows that good correlation can still be attained between the scale flux and blue quadrant sensor flux *(figure 36)*.

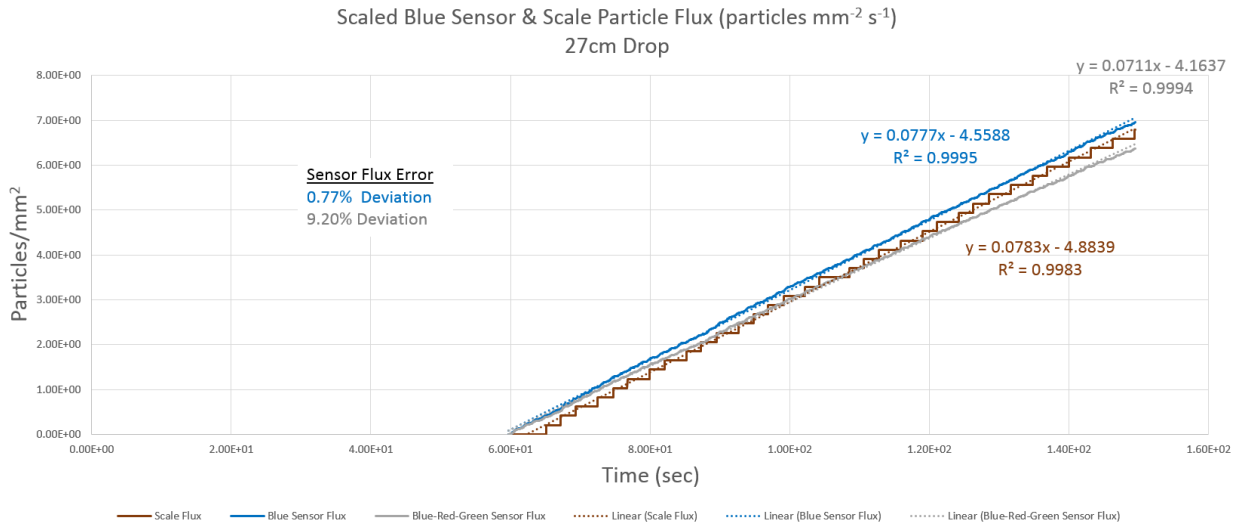

Figure 36 *– Flume drop flux test using blue sensor quadrant and corrective scaling.*

It can also be seen from a subsequent wind tunnel test performed after balancing the gains and offsets in the signal conditioner hardware for each of the sensor quadrants, that excellent agreement between the scale flux and the blue quadrant sensor flux can be achieved with the same scale factors *(figure 37)*. In retrospect, a calibration procedure for matching the sensitivity of the sensor quadrants should have been implemented as part of the construction process of the saltation sensor. Several sensor quadrants would have been constructed and grouped according to the closeness of match between their sensitivity levels. This procedure would insure the absence of outliers amongst the four quadrants of the saltation sensor as demonstrated with the current sensor and would preclude the need to generate a calibration file for each sensor. Nevertheless, if very precise agreement with a calibration standard is required, a calibration file for each sensor quadrant would provide a solution.

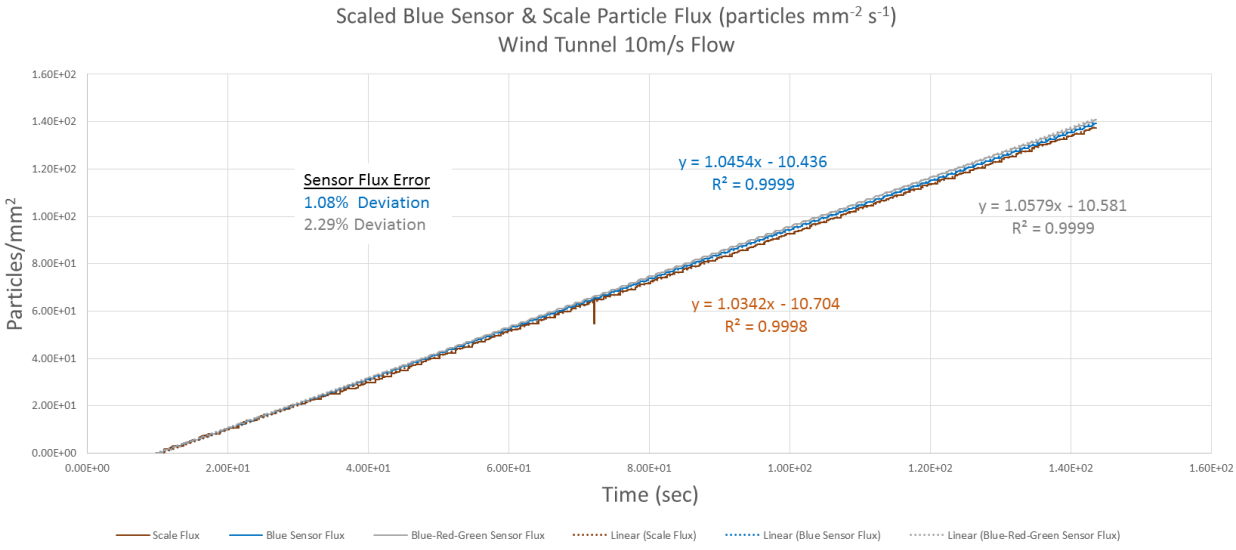

Figure 37 *– Wind tunnel flux test using blue sensor quadrant and corrective scaling.*

Wind Tunnel Energy Tests

The saltation sensor will be exposed to wind-blown particles lifted from the Martian regolith. Therefore, energy testing within the wind tunnel provides more realistic simulations of the conditions on the Martian surface. One of the first tests performed in the wind tunnel sought to verify that the saltation sensor was impervious to wind forces that could generate false impact readings. This requirement was satisfied by exposing the saltation sensor to a moderate velocity *(15 m/s),* particle free wind stream without recording any impacts. Subsequent wind tunnel tests sought to verify that energy measurements could be performed in conditions where particle trajectories are altered by wind forces. This contrasts the gravity-drop flume arrangement where nearly all of the particles move parallel to the gravity vector causing the averaged energy measurement to diminish as more impacts with larger tangential components are included *(figure 38)*. The sensor only reacts to the velocity component of the particles that are normal to the surface: tangential components are ignored. This phenomenon becomes more interesting in the presence of wind because it causes many of the particles to flow tangentially instead of normal to the sensor. In fact, there is a point along the sensor surface beyond which the velocity vectors of the impinging particles remain strictly tangential to the cylindrical sensor surface as shown in the computational flow diagnostic simulation *(figure 39)*. This is similar to the condition when the particles are impacting the edges of the sensor during the gravity-drop flume test: there is no normal velocity component. Consequently, information obtained from the gravity-drop flume test can be leveraged to determine some characteristics of the energy test results from the wind tunnel. Therefore, we begin by examining the energy test results from the gravity-drop flume tests.

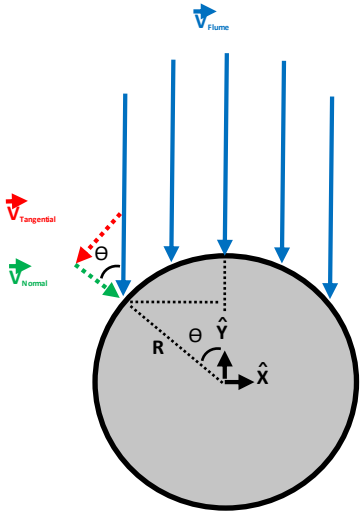

Figure 38*– Particle velocity vectors shown for gravity-drop flume test.*

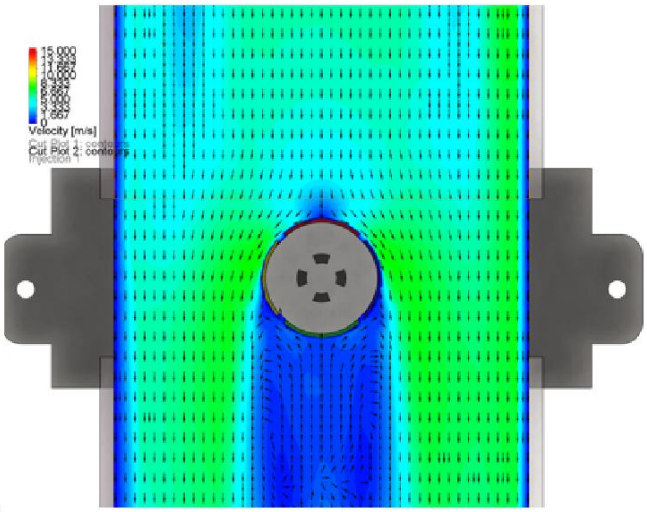

Figure 39 *– CFD simulation of particle flow around saltation sensor in 10m/s wind.*

The averaged energy of the particle impacts over a specified area of the sensor during a gravity-drop flume test can be calculated using particle velocity, particle mass and the geometry of the sensor *(figure 19b).* First, the component of the particle velocity normal to the sensor surface *(figure38)* is calculated using equations 6 and 7.

$$V_{Normal} = V_{Flume}\cos\Theta \qquad \Theta = \sin^{-1}\frac{x}{R}$$

$$V_{Normal} = V_{Flume}\cos\left(\sin^{-1}\frac{x}{R}\right) = V_{Flume}\sqrt{1-\left(\frac{x}{R}\right)^2}$$

Equations 6 & 7

Then the averaged normal component of the particle velocity "V_{Normal}" is calculated *(equation 8)* which reduces to a constant "τ_{Flume}" times the velocity of the particle flow "V_{Flume}". The upper bound of the integral used to calculate the average magnitude of the particle velocity normal to the sensor surface is denoted as a fraction of the sensor radius "βR" ranging from zero to R. In this way, the average velocity measurement can be calculated for any angular sector "Θ" of the sensor. Afterward, the scale factor τ_{Flume} can be expressed in terms of β_{Flume} *(Equation 9)* which is calculated using the saltation sensor geometry *(equation 10).*

$$\bar{V}_{Normal} = \frac{V_{Flume}}{\beta R^2}\int_0^{\beta R}\sqrt{R^2 - x^2}\,dx = \tau_{Flume} V_{Flume}$$

$$\tau_{Flume} = \frac{1}{\beta R^2}\int_0^{\beta R}\sqrt{R^2 - x^2}\,dx = \frac{1}{2}\left(\sqrt{1-\beta^2} + \frac{\sin^{-1}\beta}{\beta}\right) \quad 1 \geq \tau \geq \frac{\pi}{4},\ for\ 0 \leq \beta \leq 1$$

$$\beta_{Flume} = \frac{x}{R} = 0.637;\ for\ x = 8.695mm,\ R = 13.65mm \quad \tau_{Flume} = 0.9275;\ for\ \beta = 0.6370$$

Equations 8,9 & 10

Also the angular sector "Θ_{Flume}" of the sensor that is actively contributing to the energy measurement can be calculated using the value of β_{Flume} *(equation 11)*.

$$\Theta_{Flume} = \sin^{-1}\frac{\beta R}{R} = \sin^{-1}\beta = \sin^{-1}(0.637) = 39.57°$$

Equation 11

The energy relationship between the averaged sensor pulse-area measurement and the averaged velocity of the particles impinging the sensor is shown in *equation 12*. Note that the gain term "g_{sand}" from *equation 4* was excluded from *equation 12* because the gains were kept constant during all wind tunnel testing and could be absorbed in the correlation coefficient. The relationship between the average energy of the particles flowing past the sensor and the averaged sensor pulse-area measurement is shown to be the product of the averaged sensor pulse-area measurement and a correlation coefficient "c_{Flume}" *(equation 13)*. The scaler "c_{Flume}" *($1.675e^{-9}$)* is formulated from the slope of the linear-fit between the averaged energies of the particles with the averaged sensor pulse areas

$$\bar{E}_{PulseAreaFlume} \propto \frac{1}{2} m \bar{V}^2_{Normal} = \frac{1}{2} m V^2_{Flume} \tau^2_{Flume}$$

$$\bar{E}_{ParticleFlume} = \bar{E}_{PulseAreaFlume} c_{Flume} = \frac{1}{2} m V^2_{Flume} \tau^2_{Flume} c_{Flume}$$

Equations 12 & 13

The wind tunnel test uses a different particle flow model where at some point along the sensor surface the particle velocity becomes tangential to the surface and remains tangential to the surface as shown in figure 40. This is in contrast to the gravity-drop flume test where the particle velocity vectors are uniformly aligned to the gravity vector *(figure 38).* The relationship between the averaged sensor pulse area measurements and the averaged velocities of the particles impinging the sensor within the wind tunnel is shown in equations 14 and 15.

$$\overline{E}_{PulseAreaWindTunnel} \propto \frac{1}{2} m \overline{V}^2_{Normal} = \frac{1}{2} m V^2_{WindTunnel} \tau^2_{WindTunnel}$$
$$\overline{E}_{ParticleWindTunnel} = \overline{E}_{PulseAreaWindTunnel} c_{WindTunnel} = \frac{1}{2} m V^2_{WindTunnel} \tau^2_{WindTunnel} c_{WindTunnel}$$

Equations 14 & 15

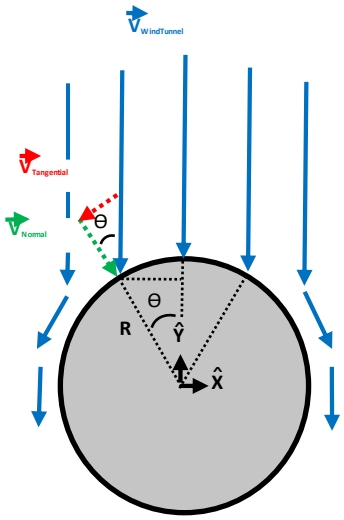

Figure 40– *Particle velocity vectors shown for wind tunnel test.*

Using the results from the wind tunnel tests as shown in *table 5*, an averaged value for "$c_{WindTunnel}$" can be obtained ($1.576e^{-9}$). This value for "$c_{WindTunnel}$" can be used to back-calculate the corresponding value for "$\tau_{WindTunnel}$". This is accomplished by setting *equations 13* and *15* equal along with their corresponding mass and velocity values and solving for "$\tau_{WindTunnel}$" *(Equation 16)*.

Sensor Quadrant	Air Speed (m/s)	Avg. Particle Velocity (m/s)	Avg. Particle Energy (joules)	Peak Area	Coefficient "$C_{WindTunnel}$"
Blue	10.0	2.74	$3.705e^{-7}$	226.9	$1.633e^{-9}$
Blue	10.0	2.87	$4.048e^{-7}$	238.4	$1.698e^{-9}$
Green	10.0	3.20	$5.037e^{-7}$	299.4	$1.682e^{-9}$
Green	10.0	2.85	$3.993e^{-7}$	283.0	$1.411e^{-9}$
Yellow	10.0	2.66	$3.502e^{-7}$	205.8	$1.701e^{-9}$
Red	10.0	2.56	$3.234e^{-7}$	242.8	$1.332e^{-9}$

Table 5 *– Wind tunnel energy results.*

The previously determined values for "τ_{Flume}", "c_{Flume}" and "$c_{WindTunnel}$" are plugged into equation 16 in order to calculate a value for "$\tau_{WindTunnel}$". Afterward, *equation 17* is set equal to the calculated value for "$\tau_{WindTunnel}$" and solved for "$\beta_{WindTunnel}$" with the aid of a commercial numerical solver.

$$\tau_{WindTunnel} = \sqrt{\frac{\tau^2_{Flume} c_{Flume}}{c_{WindTunnel}}} = 0.9562; \quad for \ \tau_{Flume} = 0.9275, c_{Flume} = 1.675e^{-9}, \ c_{WindTunnel} = 1.576e^{-9}$$

Equation 16

$$\tau_{WindTunnel} = \frac{1}{2}\left(\sqrt{1-\beta^2} + \frac{\sin^{-1}\beta}{\beta}\right) = 0.9562\,;\ solve\ for\ \beta,\ \beta_{WindTunnel} \cong 0.5023 \quad \text{Equation 17}$$

The fraction "$\beta_{WindTunnel}$" determined by equation 17 is used to calculate the angular sector "$\Theta_{WindTunnel}$" of the sensor that is actively contributing to the energy measurement while exposed to the wind conditions within the tunnel *(Equation 18)*.

$$\Theta_{WindTunnel} = \sin^{-1}\left(\beta_{WindTunnel}\right) = \sin^{-1}\left(0.50227\right) = 30.15^{\circ} \quad \text{Equation 18}$$

The resulting calculation of "$\Theta_{WindTunnel}$" suggests that the impact measurements within the wind tunnel are effectively averaged over a smaller angular region of the sensor surface where particles have normal velocity components with higher magnitudes. Under these circumstances, the averaged particle energy measurement across the surface of the sensor moves closer to the actual average of the particle energy within the flow. As a result, the wind tunnel test results yield a smaller correlation coefficient "$c_{WindTunnel}$" for determining the average particle energy than that of the gravity-drop flume test "c_{Flume}". This observation is also highlighted by the comparison of the calculated "active" angular sectors for the gravity-drop flume test "Θ_{Flume}" (39.57°) and wind tunnel test "$\Theta_{WindTunnel}$" (30.15°) where a 9.42° deviation is shown. The smaller active angular region for the wind tunnel test implies that the wind is causing the particles to go "tangential" at a point before reaching the physical ends of the relevant sensor quadrant, thereby increasing the averaged measured energy level of the particle flow. The simulated flow lines generated by the CFD analysis show the feasibility of these assertions (figure 41).

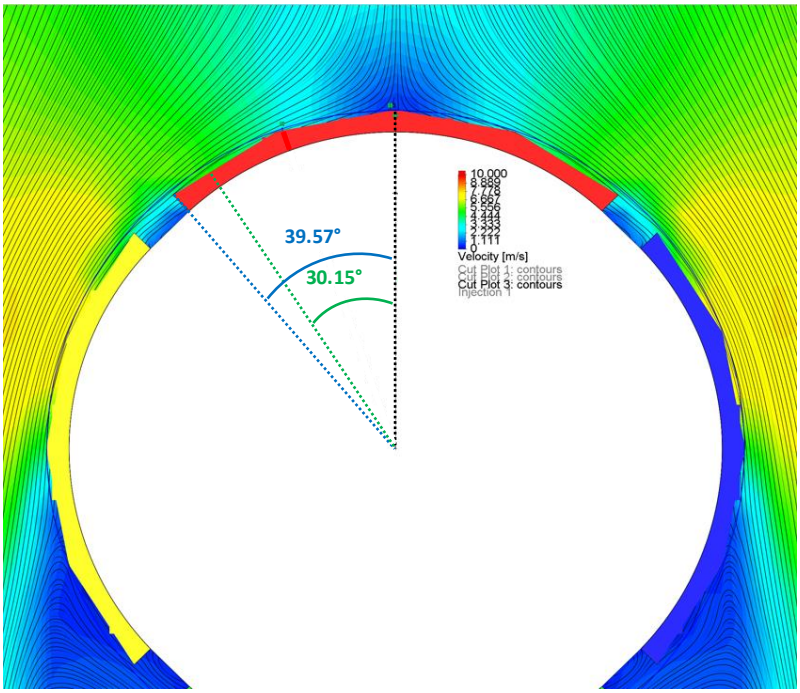

Figure 41–*Magnified view of CFD simulated flow lines around saltation sensor. Blue sector represents gravity-drop flume test active region and Green sector represents wind-tunnel test active region.*

The behavior of the particle flow around the cylindrical shape of the saltation sensor can be characterized by a dimensionless quantity known as the Reynolds number "R_e". The characteristics of the flow remain the same for Reynolds numbers within a specified ranges *(Goharzadeh, Molki, 2014) (figure 42)*.

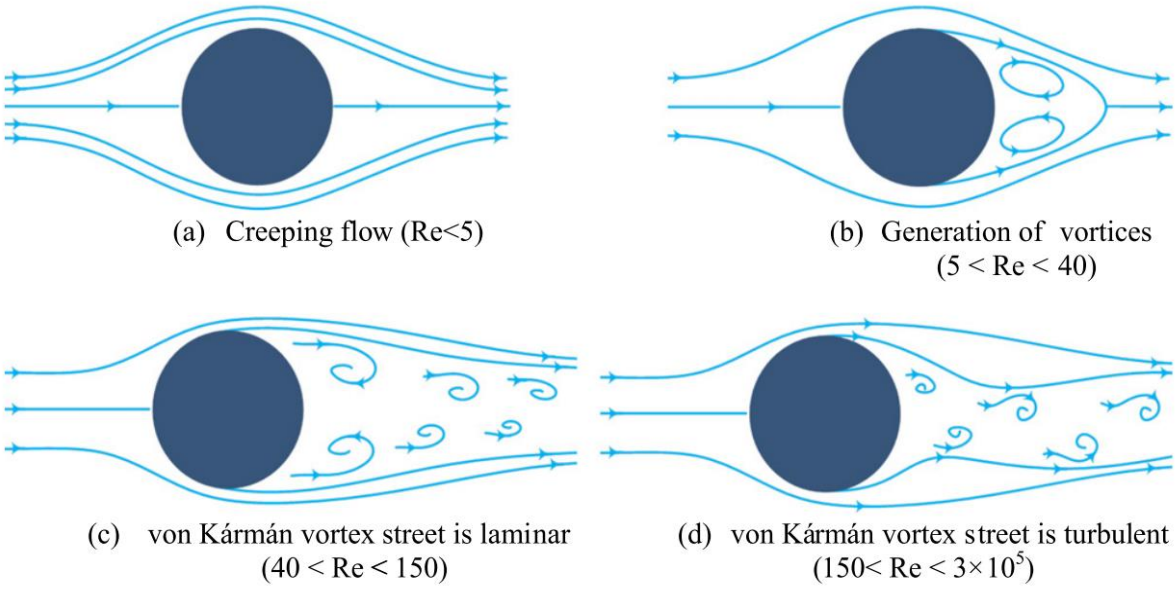

Figure 42– *Particle flow characteristics for various ranges of Reynolds numbers (Goharzadeh, Molki, 2014).*

Therefore, a wind tunnel test that mimics the environmental conditions required to stay within a particular range of Reynolds numbers would produce data that would yield a correlation coefficient "$c_{WindTunnel}$" useable in a similar environments. The wind tunnel tests performed earlier yielded a Reynolds number of 1.75×10^5 *(table 8)* which can be obtained using *equations 19-21* in conjunction with *table 6 (Gas=Air)* and *table 7 (Environment=Earth) (Tan, 2014)*.

$$R_e = \frac{\rho U D}{\mu} \qquad \left.\begin{array}{l} U = (particle\ flow velocity\ m s^{-1}) \\ D = (diameter\ of\ cylinder) = 0.273\ m \end{array}\right\} \text{Equation 19}$$

$$\rho = (density\ Kg\ m^{-3}) = \frac{P}{R_{Specific} T} \quad \Big\} \text{Equation 20}$$

$$\mu = (dynamic\ viscosity\ Kg\ m^{-1} s^{-1}) = \mu_0 \left(\frac{T_0 + T_S}{T + T_S}\right)\left(\frac{T}{T_0}\right)^{3/2} \quad \Big\} \text{Equation 21}$$

Environment	P (Pa)	T (K)	$R_{Specific}$ (J/Kg K)
Earth (Air)	1.01325×10^5 (1 atm)	297.04 (75°F)	286.9
Mars (CO_2)	600	215→218 (-72.7°F → -67.3°F)	188.9

Table 6 *– Parameters used in the calculation of the gas density ρ of Air and CO_2.*

Gas	T_S (K)	T_0 (K)	μ_0 (10^{-6} Pa s)
Air	120	291.15	18.27
CO_2	240	293.15	14.8

Table 7 *– Parameters used in the calculation of the dynamic viscosity μ in Air and CO_2.*

This Reynolds number reflects flow characteristics that produce a turbulent Von Karman vortex street as shown in *figure 42*. If the average Martian environmental parameters *(Catling, 2009), (Williams, 2016)* from *tables 6 & 7 (Gas=CO2, Environment=Mars)* are used in the equations to calculate the Reynolds number *(equations 19-21),* a range of Reynolds numbers from 720 to 3703 are obtained *(table 8)*. Once again, these Reynolds numbers reflect the same flow characteristics as the wind tunnel test where turbulent Von Karman street behavior is observed. Consequently, the correlation coefficient "$c_{WindTunnel}$" would be the same as the correlation coefficient on Mars "c_{Mars}" during nominal atmospheric conditions.

Environment	U (m/s)	R_e
Earth	10	1.75×10^5
Mars	2→10	720→3703

Table 8 *– Parameters used in the calculation of the Reynolds numbers for the wind tunnel and Mars.*

This implies that particle energy calculation can be successfully executed despite variations in pressure, temperature and wind velocity on the Martian surface because the flow characteristics remain nominally the same throughout a typical range of atmospheric conditions. Consequently, the energy measurements can be made without additional instruments used to acquire the air density and wind velocity; quantities required to determine the Reynolds number. If widely varying atmospheric conditions resulted in different particle flow characteristics around the saltation sensor, a method of determining the Reynolds number would be necessary in order to select the corresponding correlation coefficient "c_{Mars}" for each of the anticipated flow behaviors. Fortunately, the particle flow characteristics can be represented with a single model thus requiring only one correlation coefficient to determine the average energy of the particle flow.

SMiRF Test Overview

The Small Multi-Purpose Research Facility (SMiRF) test of the Martian Aqueous Habitat Reconnaissance Suite *(MAHRS)* saltation sensor was performed to satisfy test requirements that were created at the start of the instrument development project. *Table 1* contains the requirements *(SALT.6.1, SALT.6.2, SALT.7.1, SALT.7.2, SALT.13)* which were verified during the SMiRF test.

The test setup for the SMiRF test is shown in *figure 43* in which the saltation sensor is enclosed in a thin walled steel box that mounts to a suspended aluminum plate. This aluminum plate is suspended from the chamber lid, with a cold wall mounted above. This cold wall disk, which is black in the image, as well as a similar cold wall in the chamber's outer wall, provides the thermal control for the chamber. A thermocouple was mounted on each of the instrument steel boxes to monitor the thermal environment near the instruments for the survival test. A second thermocouple was added to each of the boxes for the operational test.

The requirements as detailed in *Table 1* yield two temperature test regimes, one for survival and another for operational testing. Consequently, the SMiRF test was done in two phases, a survival test, and an operational test. The survival test subjected the test articles to conditions similar to what an exposed instrument part would be subjected to, which is -128°C to +50°C. The survival test only tested the portion of the assembly which would be externally mounted; that is the saltation probe and not the supporting electronics. In contrast, the operational testing subjected the test articles to temperatures and pressures an instrument would see while housed within the heated interior of rover which is -40°C to +50°C. This operationally tested all internally housed components of the saltation sensor. During the operational test, the power and communication wiring harness was connected to the saltation electronics.

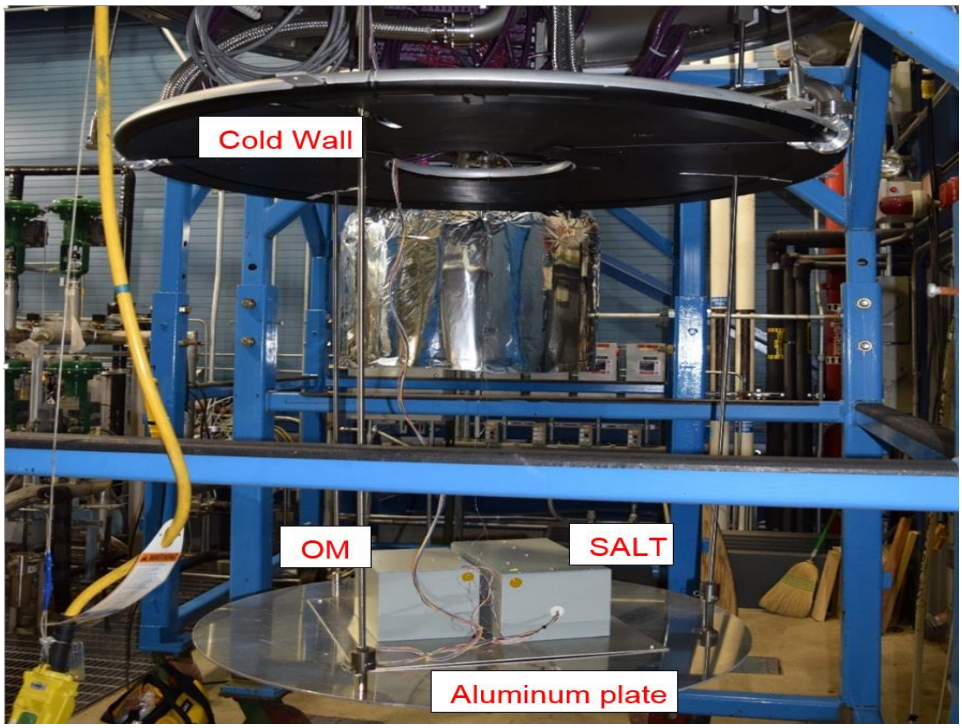

Figure 43 *- SMiRF test setup. The instruments (Saltation Sensor-SALT, Optical Microscope-OM) are mounted inside the steel boxes which are mounted to the hanging platform. This platform is near the middle of the cold wall within the chamber.*

Survival Testing

Thermal cycling and exposure to the extreme temperatures of the Martian surface were of major concern for the instruments. The saltation sensor was exposed to the extreme temperatures of the Martian atmosphere *(figure 44)*. While the saltation probe was constructed of materials specified for the Martian ambient temperature range, there was a concern that differences in materials thermal coefficients of expansion may result in the epoxy of the probe to fail, allowing the components to separate. This epoxy separation would result in the probe working incorrectly. *Figure 45* shows the pressure and temperature profile of the SMiRF survival test as performed for step 5 of the test.

Survival testing of the saltation probe consisted of:

1. Capturing data from the saltation probe
2. Removing the saltation probe from saltation electronics
3. Inspecting and photographing saltation probe
4. Installing the saltation probe in the SMiRF test setup, and then chamber
5. Performing SMiRF environmental pressure and temperature profile
6. Removing the saltation probe from the SMiRF test setup
7. Inspecting and photographing saltation probe
8. Connect the saltation probe to the saltation electronics and take data

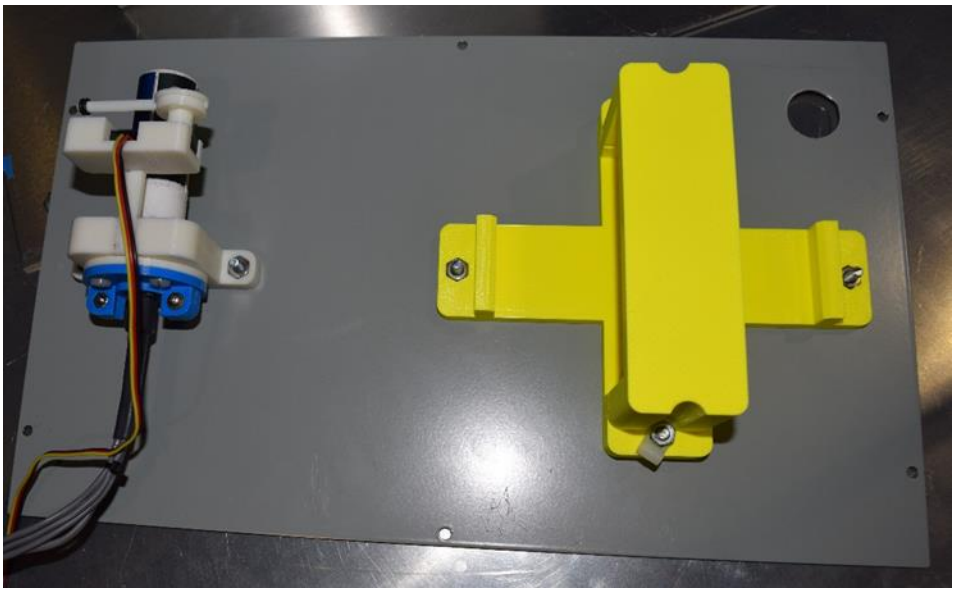

Figure 44 - Saltation sensor probe and test exciter post survival test.

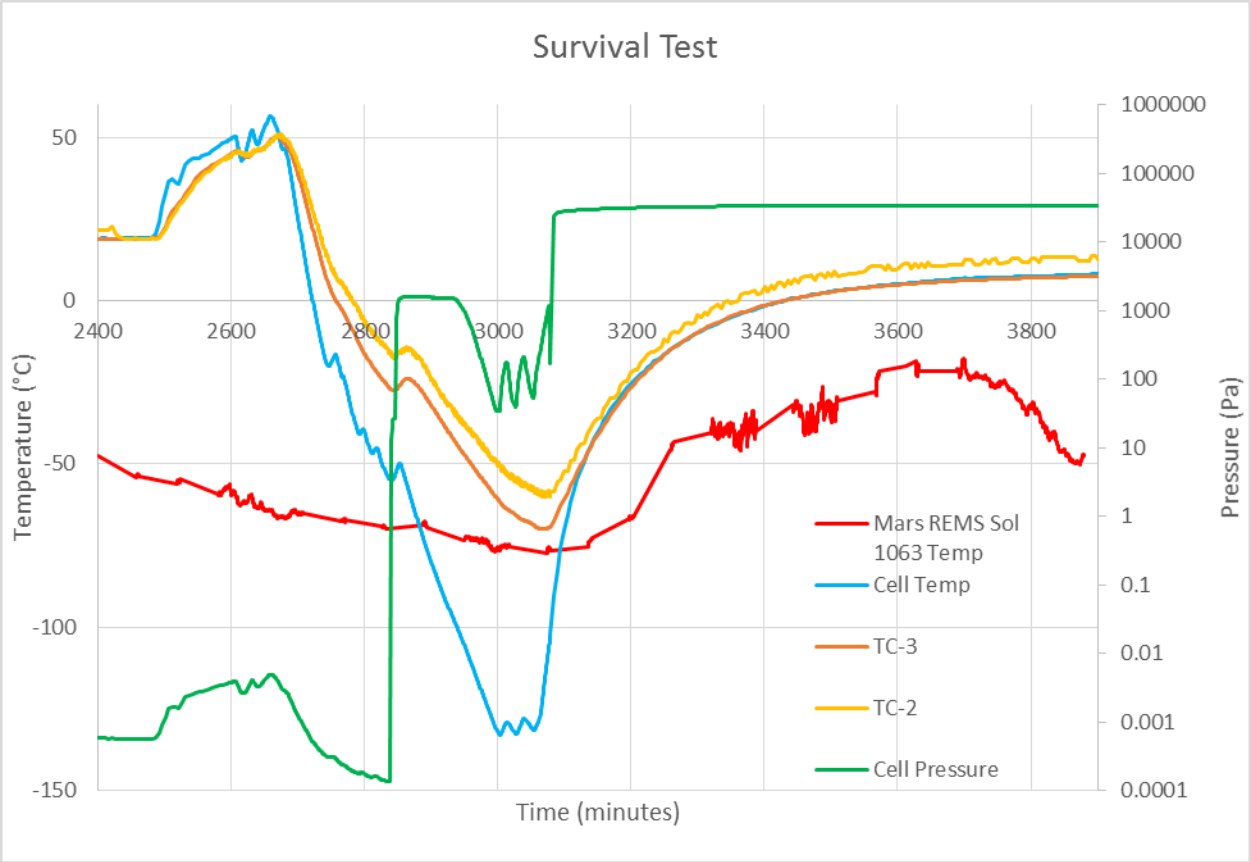

Figure 45 *- Survival Test Environmental Data.*

Operational Testing

The setup of the operational test differed from the survival test in that the entire instrument assembly was installed in the SMiRF chamber. Additionally the instruments were powered and data was taken. The saltation sensor was excited through the use of a Shape Memory Alloy (SMA) actuated hammer. This hammer was actuated to ping the saltation probe, providing an impact to measure as shown in *figure 46*.

Operational testing of the saltation probe and electronics consisted of:

1. Installing the saltation sensor and electronics in the SMiRF chamber.
2. Taking the initial data set at room temperature and pressure.
3. Performing SMiRF environmental pressure and temperature profile, taking data throughout the Mars surface temperature range as shown in Table 9.
4. Removing and inspecting the saltation probe and electronics.

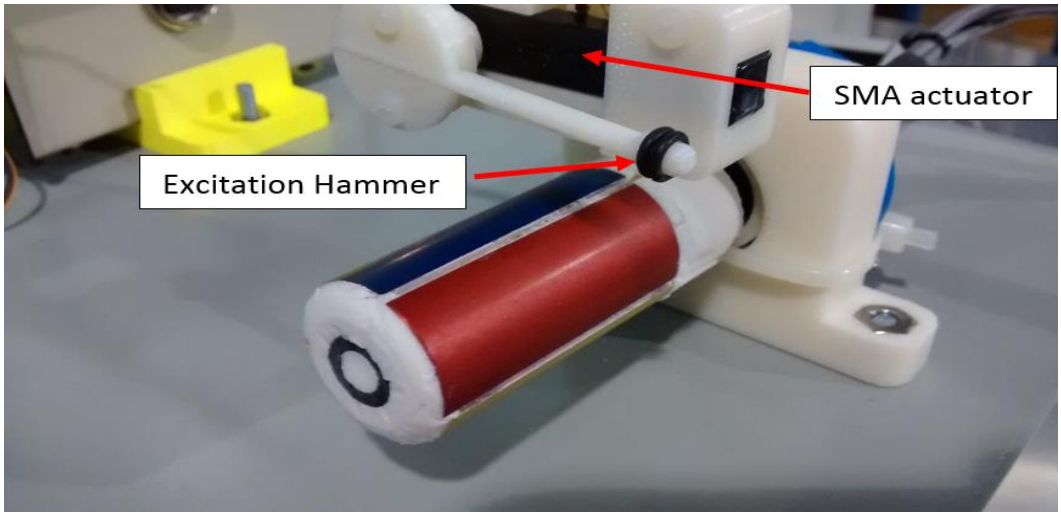

***Figure 46** - Saltation probe attached to steel box lid, post survival test, prior to installation in box for operational test.*

	Temperature	**Pressure**	Requirement
Mars Surface Hot	+50°C	Mars (12Torr, 1.6kPa)	4/5/7.1/7.2/13/24
Mars Surface Cold	-40°C	Mars (12Torr, 1.6kPa)	4/5/7.1/7.2/13/24
Transit	-40°C	Vacuum(10e-5 Torr, 0.013Pa)	6.1
Transit	-+50°C	Vacuum (10e-5 Torr, 0.013Pa)	6.1

***Table 9** - SMiRF Test operational test environmental parameters.*

SMiRF Test Results

The saltation sensor appeared unchanged in post survival test inspection and testing. Once the survival test was complete, the saltation sensor was assembled and installed for the operational test. *Figure 47* shows the SMiRF operational test pressure and temperature data. The red diamonds show when the saltation sensor data was taken. TC-3 and TC-4 were the temperatures measured on the enclosure box for the saltation sensor. Test readings showed that the saltation sensor reached over 72°C, which is outside the operational temperature range. The temperature exceeded the planned test limits because the chamber temperature was operating under open loop control and was left idle overnight. The facility operators did not expect the chamber temperature to rise to that level. However, the saltation sensor was successfully operated in vacuum at the extreme limits of the test temperature range throughout the operational test. Calibrated instrument performance was unable to be measured during the environmental test as there was no calibrated excitation source for the instrument. The operational test showed that the SMA actuator used to ping the saltation sensor had sufficient energy to excite all four quadrants of the saltation sensor even though the red quadrant was the only surface actually impacted by the hammer.

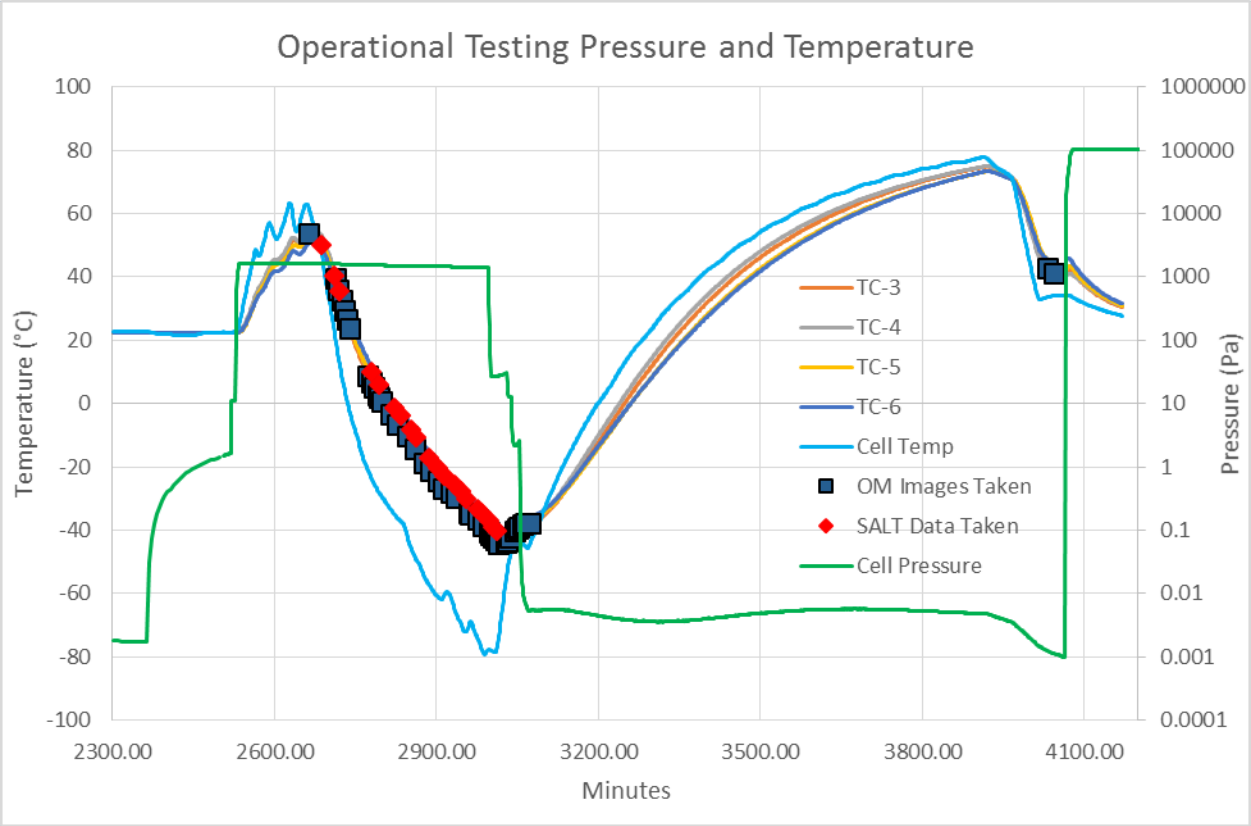

Figure 47 *- SMiRF Operational Test Environmental Data of the saltation sensor (SALT).*

Figure 48 shows the four quadrant signals of the saltation sensor plotted for different temperatures. The plots are color coded to the corresponding sensors quadrants. Energy is plotted on the y-axis and time on the x-axis. The energy of the strikes on the surface of the red quadrant is proportional to the height of the red curve pulses. At colder temperatures the excitation appeared to saturate the sensor resulting in the flat pulses in the beginning of the curves. This saturation phenomenon is expected if the excitation exceeds the capacity of the sensor's conditioning circuitry. Later in the acquisition timeline (right side of graphs), the input saturation would relax and trailing pulses can be seen. This phenomenon is more easily seen in *figure 49*.

Temperature had a major effect on the saltation sensor test results primarily because the SMA actuates by heat induced shape changing. In fact, it was observed that the hammer took a significantly longer period of time to retract as the temperature in the chamber increased. Consequently, the automated pulsing circuit that drove the SMA actuator during the high temperature periods of the testing within the SMiRF chamber could no longer be used. As the chamber temperature was elevated, the fixed pulse time became too short to allow the hammer to significantly retract from the surface of the sensor. Consequently, during the higher temperature periods of the testing, the SMA actuator was given a minimum of 60 seconds after each impact before it was manually triggered again to get the next measurement. Once the chamber temperature was lowered again, the sensor plots would repeatedly return to a nominal signature profile which would tend to indicate that the piezo-electric sensor and RTV were not affected by the temperature and pressure variations within the SMiRF chamber. Nevertheless, this test could not show that saltation sensor measurements were impervious to temperature variations throughout the entire range because the temperature effects from the SMA actuator cannot be separated from the acquired sensor data.

However, the test results did show that sensor measurements remained consistent through a sub range of the operating temperatures, despite any changes in the SMA actuator operation. *Figure 49* shows the red face signal after impact by the SMA hammer for the lower range of temperatures from the operational test (-40°C to -20.4°C). In this range of temperatures, the sensor and SMA exciter operated similarly throughout the range. The sensor saturates for the same time constant which is the flat step at the beginning of the graph, and then exhibits four "echoes" through the time sampling period. These "echoes" are likely due to either a traveling wave propagating through the sensor caused by the initial excitation of the hammer impact, or multiple impacts from the hammer bouncing. If the peaks of the echoes are compared to each other, they are within an average of 27% of each other from -40°C to 0°C which indicates comparable sensor behavior within this temperature range.

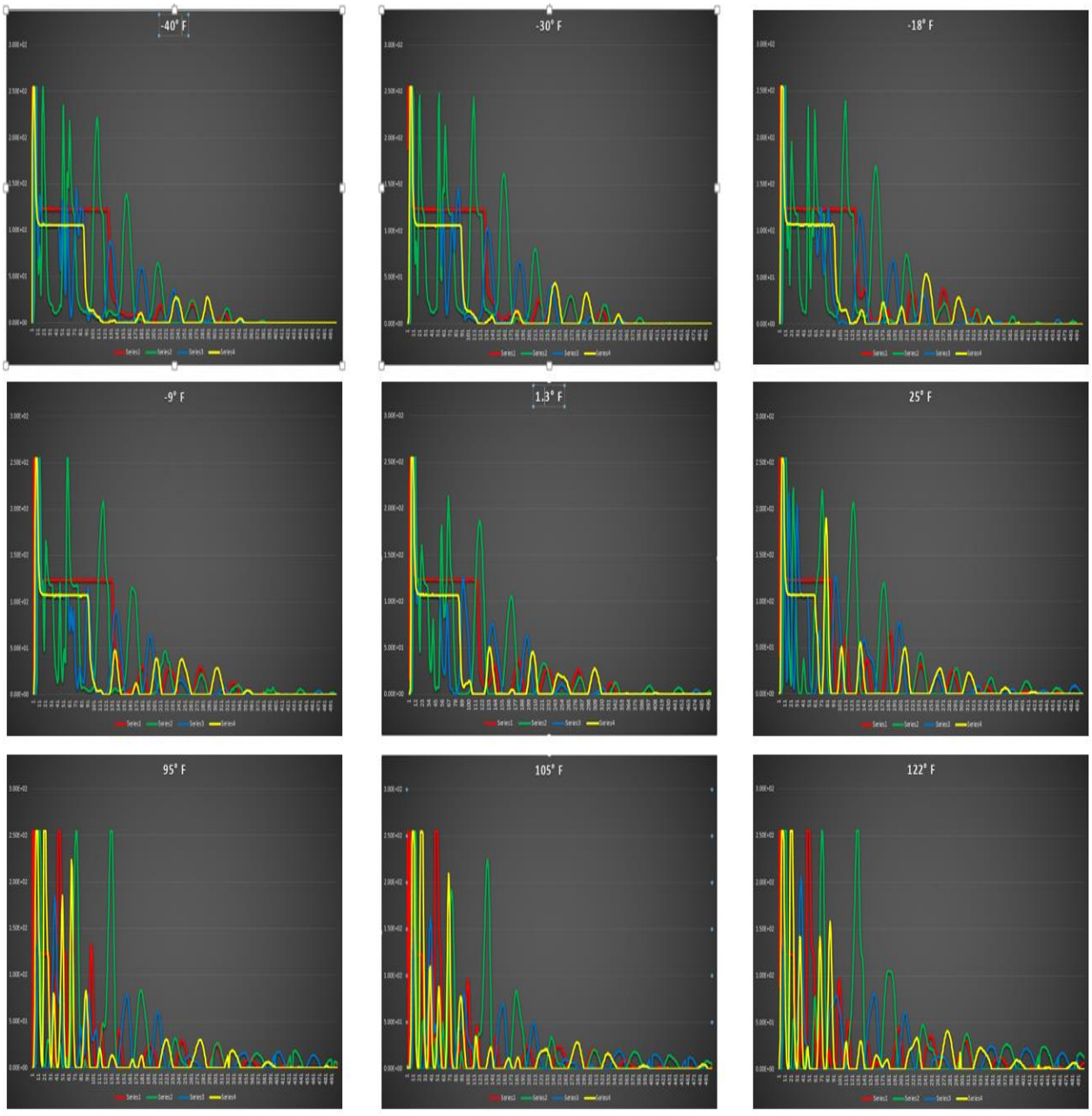

Figure 48 *- Saltation sensor ping results from operational test.*

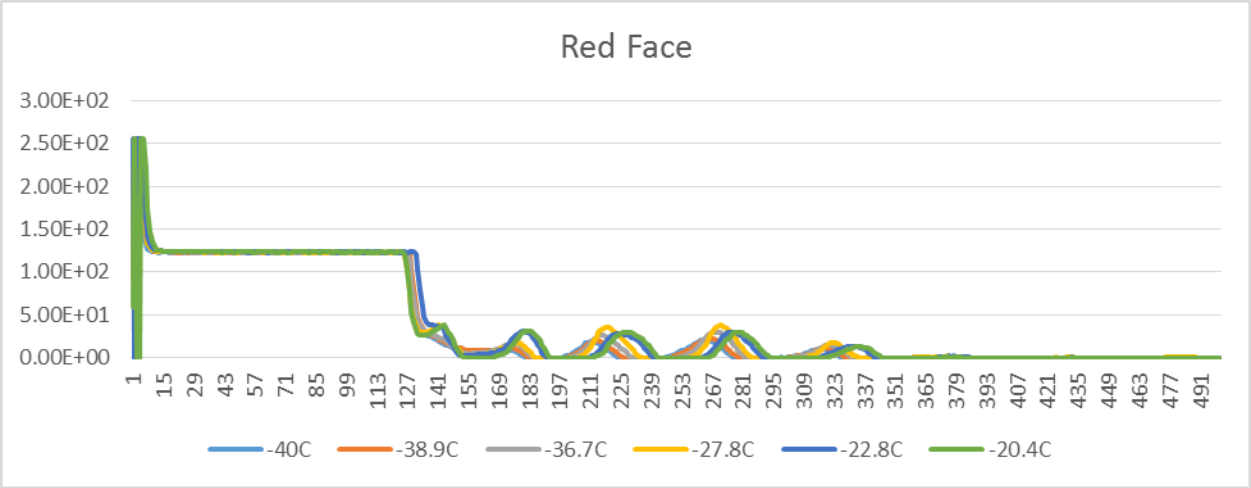

Figure 49 *– Impacts on red quadrant of the saltation sensor as a function of temperature.*

Conclusion

Wind-tunnel and gravity-drop flume testing showed that the saltation sensor can accurately record the flux rate, total count, averaged kinetic energy and direction of a particle flow. The saltation sensor also demonstrated its invulnerability to wind and electromagnetic interference. Environmental testing revealed that the sensor possesses a wide operational temperature and pressure range suitable for Mars missions. The test results also clarified the design of the saltation sensor electronics and firmware. Specifically, calculating the particle energy by exclusively using the pulse area (more effective than using the pulse peak), adding the energy spectrum analyzer to the measurement suite, increasing the width of the counter registers from 16 to 32 bit, adding counter overflow indicators and improving the interrupt scheme used to initiate signal acquisition when above the designated threshold. In addition to hardware and firmware improvements, the testing highlighted areas in the construction process of the saltation sensor that warrant attention, particularly the addition of a sensor quadrant matching process. Such a process would insure equivalence in the signal responsiveness of each of the four quadrants of the saltation sensor. Furthermore, the future build process should eliminate the recessed gaps between the quadrants. This would reduce turbulent flow across the surface of the sensor and prevent sand particles from getting trapped in the recesses.

References

Goharzadeh, A., Molki, A., 2014. Measurement of fluid velocity development behind a circular cylinder using particle image velocimetry (PIV). European Journal of Physics, Volume 36, Number 1

Baas, A.C.W., 2004. Evaluation of saltation flux impact responders (Safires) for measuring instantaneous aeolian sand transport intensity. Geomorphology 59. 99-118

Barchyn, T.E., Hugenholtz, C.H., 2010. Field comparison of four piezoelectric sensors for detecting Aeolian sediment transport. Geomorphology 120. 368-371.

Catling, D.C., 2009. Atmospheric Evolution of Mars. In: V. Gornitz (ed.) Encyclopedia of Paleoclimatology and Ancient Environments, Springer, Dordrecht, pp. 66-75.

Glynn, E.F., 2010. USAF 1951 and Microcopy Resolution Test Charts and Pixel Profiles. Efg's Computer Lab., www.efg2.com/Lab/ImageProcessing/TestTargets/#USAF1951.

Intelligent® Weighing Technology., 2009. Intell-Count™ Dual Channel Counting Scale IDC Series, User Operation Manual. www.intelligentwt.com.

Kok, J.F., 2010. Difference in the Wind Speeds Required for Initiation versus Continuation of Sand Transport on Mars: Implications for Dunes and Dust Storms. Physical Review Letters 104, 074502.

Kok, J.F., Renno, N.O., 2006. Enhancement of the emission of mineral dust aerosols by electric forces. Geophysical Research Letters, Vol. 33, L19S10.

Sensit™., 2013. Data Processing & Calibrations. TM-H14-LIN., http://www.sensit.com/images/TM-H14-LIN_July062014.pdf

Sherman, D.J., Li, B., Farrell, E.J., Ellis, J.T., Cox, W.D., Maia, L.P., Sousa, P.H.G.O., 2011. Measuring Aeolian Saltation: A Comparison of Sensors. Journal of Coastal Research, Number 10059. 280-290.

Tan, Z., 2014. Air Pollution and Greenhouse Gases from Basic Concepts to Engineering Applications for Air Emission Control. Springer XXVIII, ISBN: 978-981-287-211-1, pp. 43-46.

Van Pelt, R.S., Peters, P., Visser S., 2009. Laboratory wind tunnel testing of three commonly used saltation impact sensors. Aeolian Research 1. 55-62.

Williams, D., 2016. Mars Fact Sheet., http://nssdc.gsfc.nasa.gov/planetary/factsheet/marsfact.html.

Wikipedia., Drag Coefficient., https://en.wikipedia.org/wiki/Drag_coefficient.

Wikipedia., Terminal Velocity., https://en.wikipedia.org/wiki/Terminal_velocity.

Hyperphysics WebSite, Freefall Velocity vs Distance for Quadratic Drag., Carl R. Nave, Department of Physics and Astronomy, Georgia State University, http://hyperphysics.phy-astr.gsu.edu/hbase/Mechanics/quadvy.html.